MATERIALS CHEMISTRY FRONTIERS

RESEARCH ARTICLE

View Article Online
View Journal | View Issue

Cite this: *Mater. Chem. Front.*, 2025, **9**, 2522

Controlled radical release from iron oxide nanoparticles grafted with thermosensitive alkoxyamine triggered by external *stimuli*†

Farah Abdel Sater,‡[a] Basile Bouvet,‡[a] Saad Sene,[a] Gautier Félix,[a] Erwan Adriaenssens,[b] Jean-Patrick Joly,[b] Gerard Audran,*[b] Sylvain R. A. Marque,*[b] Joulia Larionova*[a] and Yannick Guari[a]

We report an investigation of a controlled radical release produced by iron oxide nanoparticles (IONPs) of *ca.* 25 nm covalently grafted through phosphonic groups with a thermosensitive alkoxyamine, (6-(4-(1-((di-*tert*-butylamino)oxy)ethyl)benzamido)hexyl)phosphonate, having a relatively low homolysis temperature (k_d = 6.4 × 10^{-4} s^{-1} at 77 °C, E_a = 117.8 kJ mol^{-1}). Action of an alternating current magnetic field (AMF) or light irradiation at 808 nm produces a rapid heating of the nanoparticles' surface, which induces the homolysis of the C–ON bond of alkoxyamines facilitating the efficient formation of free radicals. We demonstrated based on homolysis kinetics investigated by electron paramagnetic resonance (EPR) spectroscopy that light irradiation at 808 nm (2.6 W cm^{-2}) enables efficient radical release from grafted nanoparticles at 44 °C ($t_{1/2}$ = 23.6 min), whereas the free molecules required 20 h to show the same release at this temperature. AMF exposure accelerates the homolysis of alkoxyamine-grafted nanoparticles (16 kA m^{-1}, 2.9 mg mL^{-1}) twofold compared to the free alkoxyamine at 77 °C ($t_{1/2}$ = 7.9 min *vs.* 18 min). These findings underscore the critical importance of localized nanoscale effects, demonstrating that the homolysis rate on the nanoparticle surface under external *stimuli* is significantly higher compared to that under external solution heating, with this enhancement being even more pronounced under light irradiation.

Received 22nd November 2024,
Accepted 25th May 2025

DOI: 10.1039/d4qm01022a

rsc.li/frontiers-materials

Introduction

Multifunctional nano-objects, capable of initiating controlled multi-step processes remotely activated by an action of external *stimuli*, have garnered a great deal of attention in recent years due to their application in the field of biology and medicine for controlled delivery of drugs, radicals, nucleic acids, siRNA or genes,[1–5] but also for enzymatic regulation,[6] separation,[7] catalysis,[8] controlled polymerization,[9] sensing,[8] *etc.* These intricate systems commonly contain inorganic nanoparticles acting as magnetothermal or photothermal nano-heaters combined with thermosensitive shells or matrixes (such as polymers, liposomes, and organic molecules) containing incorporated or attached payload. When subjected to the remote action of light irradiation (photothermal activation) or an alternating magnetic field (AMF) (magnetic stimulation), these nanoparticles show localised temperature increase near their surface, which, in turn, activates the transformation of thermosensitive moieties and therefore delivery of payload. This so-called cascade multi-step strategy excels over a conventional single-functional approach, demonstrating superior controllability, specificity, efficiency of actions and often synergistic effects.

Among different inorganic nano-objects used as remotely activated nano-heaters, iron oxide nanoparticles (IONPs) are the mostly investigated in the literature since their composition, size, morphology, surface state and therefore their heating properties can be precisely controlled.[10] Indeed, they can efficiently convert electromagnetic energy into heat upon exposure to AMF in the 100–350 kHz radiofrequency range with a few tens of kA m^{-1} field intensity.[11] While investigated for numerous decades, the recent years have witnessed extensive development of a new generation of magnetic IONPs with various morphologies, featuring improved magnetic properties, making them efficient as magnetothermal nano-heaters with high specific absorption rate (SAR) values.[12–16] Moreover, IONPs have recently been investigated as rather interesting

[a] *ICGM, Univ. Montpellier, CNRS, ENSCM, CNRS, Montpellier, France. E-mail: joulia.larionova@umontpellier.fr, yannick.guari@umontpellier.fr*
[b] *Aix Marseille Univ, CNRS, ICR, UMR 7273, Avenue Escadrille Normandie-Niemen, 13397 Marseille CEDEX 20, France. E-mail: g.audran@univ-amu.fr, sylvain.marque@univ-amu.fr*

† Electronic supplementary information (ESI) available. See DOI: https://doi.org/10.1039/d4qm01022a

‡ These authors equally contributed to this work.

photothermal agents within the near-infrared (NIR) window, as they effectively convert light into thermal energy.[17,18]

Of the various employment of smart nano-systems involving multistep processes, the controlled release of radicals and/or reactive oxygen species (ROS), triggered by photothermal, magnetothermal, enzyme and other actions, holds particular promise in the biomedical area and materials science.[19–23] On the one hand, they present unique advantages for biomedical applications over classical drug delivery systems due to selective and very local cytotoxicity, capitalizing on the inherent ability of radicals to induce targeted damage to cancer cells or bacteria while sparing normal tissues. Additionally, the mechanisms of action differ significantly from those of traditional drug release systems and are promising to overcome challenges associated with drug resistance. Moreover, the combination of remotely activated heating and radical delivery introduces synergistic effects, creating a dynamic interplay that elevates the overall efficiency and specificity of the therapeutic action. On the other hand, some of these systems enable nanoparticle-assisted controlled radical polymerization, offering the creation of intricate polymer-based materials.[9,24,25] This method can be especially beneficial in situations where classical radical polymerization methods falter including the employment of highly reactive monomers, requirements for precise control over surface functionalization, the challenging design of complex polymer architectures, and the synthesis of intricate hybrid materials. The literature analysis indicates that the majority of systems offering the nanoparticle-assisted delivery of radicals/ROS involve the presence of oxygen-rich environments. However, the generation of oxygen-independent free radicals offers a pivotal advantage in various scenarios, including the hypoxic conditions prevalent in tumours, some environmental remediation or industrial polymerization reactions. In this regard, intense research activities have been carried out over the past few years, based on a strategy of combining an alkyl radical generator with an organic[26] or inorganic nano-heater.[27] Among these, there are notably oxide nanoparticles (iron oxides,[28] MnO_2[29]), sulphides (Bi_2S_3,[30] CuS,[31] $CuFeS_2$,[32] FeS_2,[33] Ag_2S[34,35]) or carbides (Fe_5C_2,[36] Nb_2C,[37]), metals (Au,[38] PdAu,[39]) and Prussian blue[40] for which the temperature elevation is triggered either by light irradiation or by application of an alternating magnetic field. This stimuli-induced heat generation leads to the activation of a radical generator which, with exceptions of peroxymonosulfate or peroxydisulfate salts,[31,41] is 2,2′-azobis-[2-(2-imidazolin-2-yl)propane] dihydrochloride (AIPH) possessing a thermosensitive azo function, thereby inducing the oxygen-independent release of alkyl radicals through a cascade process. To the best of our knowledge, IONPs have been relatively scarcely investigated to design nano-systems able to release radicals in a multistep cascade fashion, where each step is regulated by a specific parameter. We can cite for instance a few works where AIPH has been inserted into the porous IONPs of 184 nm[28] or co-loaded with small spherical 10 nm IONPs into large polymer nanoparticles.[42] However, it should be noted that in these works, the radical initiators were simply inserted and not covalently linked to the hosting nanoparticles, leaving some inconvenience or risks compromising efficiency, including possible molecules' leaching into the surrounding environment, limited stability over time, the limited precision in efficiency to trigger mechanisms, *etc.*

Alkoxyamines present an interesting alternative to AIPH or sulphate derivatives as a source of radicals. Indeed, these organic molecules of the general formula $R_1R_2NOR_3$ possess a homolysable C–ON bond, which can be cleaved upon an activation, generating therefore two radical species, alkyl ($^{\bullet}R_3$) and nitroxyl ($R_1R_2NO^{\bullet}$) radicals.[43] They offer unique advantages, including tunable activation energy and important stability. Various types of the C–ON bond activation for free alkoxyamine molecules have been investigated, including chemical activation, light irradiation or thermal heating.[44] The lability of the C–ON bond in alkoxyamines depends on different factors,[45–47] which can be modulated to create stable alkoxyamine molecules with adjustable activation energy and, therefore, tuneable homolysis temperatures.[43] Moreover, alkoxyamines can be functionalized with specific moieties enabling to coordinate with the surface of nanoparticles.

Recently, we reported the first example of magnetic IONPs of *ca.* 25 nm covalently grafted with a thermosensitive radical initiator alkoxyamine, (6-{4-[1-(2,2,6,6-tetramethyl-piperidin-1-yloxy)-ethyl]benzoylamino}-hexyl)-phosphonate.[48] These nanoparticles were able to provide a controlled delivery of radicals in *tert*-butylbenzene at around 100 °C remotely triggered by an application of AMF. Encouraged by these promising results, we extended our investigations to another alkoxyamine derivative, (6-(4-(1-((di-*tert*-butylamino)oxy)ethyl)benzamido)hexyl) phosphonic acid, which is expected to exhibit a lower activation energy barrier and, consequently, more efficient radical generation under thermal activation, allowing either faster homolysis or activation at lower temperatures, while maintaining good stability at room temperature.

In this article, we report on design of new nano-objects consisting of IONPs covalently grafted with (6-(4-(1-((di-*tert*-butylamino)oxy)ethyl)benzamido)hexyl) phosphonate and investigations of their radical release ability under external stimuli. Alongside investigation of magnetothermal activation of our system under different conditions (nanoparticle concentrations, AMF parameters, and solvents), we also focused on exploring photothermal triggering under light irradiation at 808 nm. The kinetics of homolysis investigated by electron paramagnetic resonance (EPR) spectroscopy indicates that light irradiation at 808 nm (2.6 W cm^{-2}) enabled efficient radical release from grafted nanoparticles at 44 °C ($t_{1/2}$ = 23.6 min), whereas the free molecule required 20 h to show the same release at this temperature. AMF exposure accelerates the homolysis of alkoxyamine-grafted nanoparticles (16 kA m^{-1}, 2.9 mg mL^{-1}) twofold compared to the free alkoxyamine at 77 °C ($t_{1/2}$ = 7.9 min *vs.* 18 min). Our results highlight the critical importance of localized nanoscale effects, demonstrating that the homolysis rate on the nanoparticle surface under external stimuli is significantly higher compared to that under bulk solution heating, with this enhancement being even more pronounced under light irradiation.

Results and discussion

Synthesis and characterisation

The synthesis of new IONP@alkoxyamine nanoparticles was performed in three steps: (i) the synthesis of an alkoxyamine derivative containing both a di-*tert*-butyl-nitroxide group with a thermosensitive C–ON bond and a pendant phosphonic acid moiety able to coordinate Fe^{2+}/Fe^{3+} ions on the nanoparticles' surface, (ii) the synthesis of the IONPs, and (iii) the grafting of the alkoxyamine through the coordination of the phosphonic acid groups to the IONPs' surface.

First, the synthesis of the alkoxyamine derivative was performed following a five-step procedure starting from the commercially available *para*-vinyl benzoic acid, which was esterified with methyl iodide (see the Experimental part). Then, the ester was coupled with di-*tert*-butyl-nitroxide radicals using Jacobsen's catalyst. The corresponding ester-alkoxyamine was hydrolysed into the carboxylic derivative, which is transformed in (6-(4-(1-((di-*tert*-butylamino)oxy)ethyl)benzamido)hexyl) phosphonate. The final step consists of hydrolysis of the phosphonate group into (6-(4-(1-((di-*tert*-butylamino)oxy)ethyl)benzamido)hexyl) phosphonic acid. All intermediate products, as well as the final alkoxyamine molecules were characterized by NMR (^1H and ^{31}P) (Fig. S1–S5, ESI†) and HRMS. The IONP/OA/OL nanoparticles stabilized by oleyl acid (OA) and oleylamine (OL) were prepared by the flash thermolysis method using the FeO(OH) precursor in *n*-docosane with an additional oxidation step (FeO into Fe_3O_4) as previously reported.[48] Finally, the post synthetic covalent grafting of the alkoxyamine derivative (6-(4-(1-((di-*tert*-butylamino)oxy)-ethyl)benzamido)hexyl) phosphonic acid to the surface of IONP/OA/OL was performed by coordination of its phosphonate groups to Fe^{2+}/Fe^{3+} ions of the IONPs' surface (Fig. 1).

Transmission electronic microscopy (TEM) images of IONP/OA/OL and IONP@alkoxyamine nanoparticles are shown in Fig. 2a and b. They indicate that the spherical morphology of the IONPs was not impacted by the alkoxyamine's grafting. Their size distributions are equal to 25.08 ± 1.61 nm and to 25.50 ± 1.90 nm, respectively (Fig. S6, ESI†). The dynamic light scattering (DLS) analysis demonstrates the fact that the obtained nanoparticles are well dispersed and not aggregated (Fig. S7, ESI†).

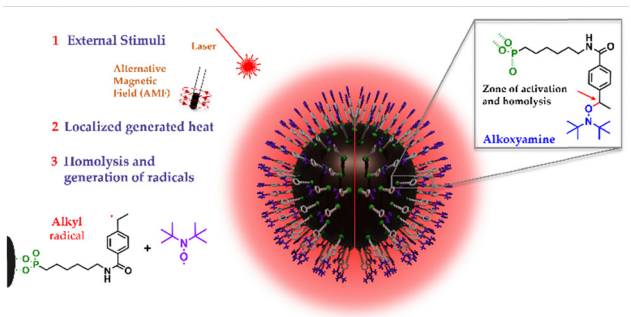

Fig. 1 Schematic representation of IONP@alkoxyamine nano-objects providing a controlled radical release triggered by external stimuli (AMF or light irradiation) in a cascade action.

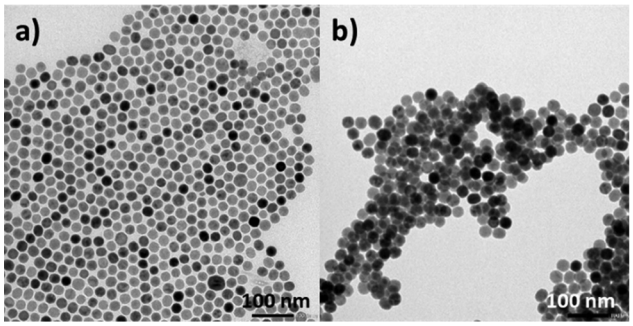

Fig. 2 TEM images of: (a) the IONP/OA/OL nanoparticles, (b) the IONP@alkoxyamine nanoparticles.

Scanning electron microscopy (SEM) coupled with EDX analysis permitted us to determine for the synthesized IONP@alkoxyamine nanoparticles the Fe/P ratio = 98.4/1.6, which indicates the successful grafting of the alkoxyamines to the nanoparticles' surface. It permits us to estimate that there are 2.6 phosphorus atom per nm^2 of IONPs. The successful grafting has been confirmed by infrared (IR) spectroscopy through the appearance of the alkoxyamine-related bands in the IR spectrum of the IONP@alkoxyamine nanoparticles when compared with those of IONP/OA/OL and the free alkoxyamine molecule (Fig. S8, ESI†). The IR spectrum of IONP@alkoxyamine shows the appearance of a stretching vibration band of the P–O–Fe bond at 1027 cm^{-1} attesting the successful coordination of the phosphonate groups to iron ions of the surface. Moreover, ν(C=O) at 1633 cm^{-1} of the alkoxyamine can also be found. The characteristic ν(Fe–O) vibration bands of iron oxide are still present at 564 cm^{-1}. The powder X-ray diffraction (PXRD) patterns of the obtained IONP@alkoxyamine nanoparticles (Fig. S9, ESI†) show the reflections, which could be attributed to the main Fe_3O_4 phase, while the minor presence of FeO or even γ-Fe_2O_3 phases cannot be excluded.[49–51] The calculated lattice constant is equal to 8.38 Å, which is in agreement with 8.39 Å of the main magnetite phase (JCPDS 19-629). The crystalline domain was calculated using the Scherrer formula obtaining an average value of *ca.* 22.4 nm.

The magnetic properties of the IONP@OA/OL and IONP@alkoxyamine nanoparticles were investigated in powdered samples using a SQUID-MPMS magnetometer working in the 1.8–350 K temperature range up to 7 T. The field dependences of the magnetization performed at 300 K for both samples are shown in Fig. S10a (ESI†). The value of the saturation magnetization is equal to 62 A m^2 kg^{-1} for both samples (before and after alkoxyamine grafting), which is lower in comparison to the value observed for the bulk pure magnetite (80 A m^2 kg^{-1}).[52] This is currently observed for IONP nanoparticles and can be explained by the presence of other phases besides magnetite with lower magnetization values (initial non oxidized FeO), which is diamagnetic and overoxidized γ-Fe_2O_3, as well as by the possible occurrence of spin frustration on the nanoparticles' surface.[49,50,53] Note that the value of the saturation magnetization is not changed after the alkoxyamine's grafting. The coercive fields at 300 K are equal to 2.2 and 13.6 mT for

IONPs and IONP@alkoxyamine, respectively. The temperature dependence of the magnetization performed in zero field cooled (ZFC)/field cooled (FC) modes under an applied static magnetic field of 100 Oe presents similar characteristics for both samples, which are typical for the IONP nanoparticles of *ca.* 25 nm with the main magnetite phase (Fig. S10b and c, ESI†). The blocking/freezing temperature determined as the maximum on the ZFC curve is situated at 371 K for the IONP@OA/OL, while it is above 400 K for IONP@alkoxyamine nanoparticles. This result may be explained by the covalent alkoxyamine grafting on the surface of the IONPs, which visibly helps to remove the surface spin frustration usually occurring for IONPs.

Magnetothermal and photothermal heating

The magneto- and photothermal properties of IONP@alkoxyamine nanoparticles were investigated to demonstrate their heating abilities triggered by either AMF or light irradiation.

Magnetothermal properties. The macroscopic heating of IONP@alkoxyamine nanoparticles was remotely activated by using AMF of 340 kHz and 20 mT (16 kA m^{-1}). A thermal camera or optical fibre, which provided similar results, was used for temperature monitoring. First of all, the temperature elevation as a function of time was investigated for colloidal solutions of different concentrations varying from 0.5 to 4 mg mL^{-1} in *tert*-butylbenzene (Fig. 3). *tert*-butylbenzene without nanoparticles was used as a reference. It did not provide any temperature elevation when subjected to the action of the magnetic field under the same conditions. In contrast, the colloidal solutions containing IONP@alkoxyamine nanoparticles induce a rapid temperature increase. On the *T vs.* time curves one can see a linear zone in the first 2 min of the AMF application and then a tendency to saturation (Fig. 3a). As an example, the temperature of 77 °C is reached after 10 min of exposure for the colloidal solution of 4 mg mL^{-1}. Note that for all concentrations the temperature remains quasi constant after 10 min when the magnetic field is maintained. Fig. 3b illustrates the variation of ΔT as a function of nanoparticles' concentration. ΔT is determined here by subtracting the initial temperature from the temperature recorded after 10 minutes of AMF exposure. As shown, ΔT increases in a linear fashion with increasing nanoparticle concentration. This indicates that the influence of dipolar nanoparticle interactions is not predominant at the concentrations under consideration.[54]

The SAR value is used to evaluate the magnetothermal performance of magnetic nanoparticles by quantifying the generated heat power under applied AMF.[11] The estimation of the SAR value was performed by fitting the whole *T vs.* time curves with a phenomenological model, incorporating a thermal exchange function developed with the second order Taylor series (see the ESI† for details).[55,56] The best fit provided the average SAR value (per g of nanoparticles) of 205 ± 1 W g^{-1} (Fig. 3). The corresponding intrinsic loss power (ILP) value, which permits the comparison of the heating capacity of nanoparticles regardless of the alternating magnetic field amplitude and frequency,[11] is equal to 2.4 nHm^2 kg^{-1}. It is

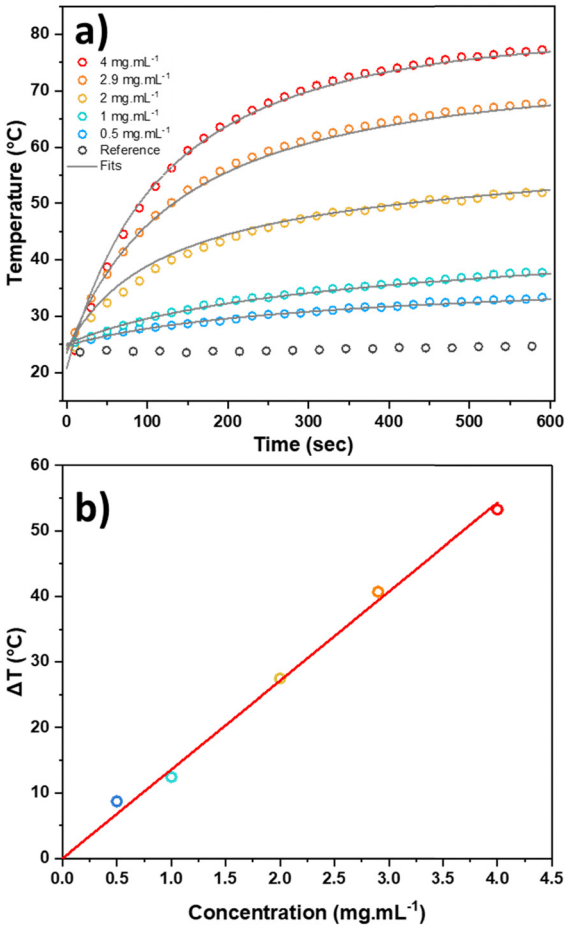

Fig. 3 (a) Temperature dependence as a function of time for different concentrations of IONP@alkoxyamine nanoparticle colloidal solutions in *tert*-butylbenzene (ranging from 0.5 to 4 mg mL^{-1}) performed under an ac magnetic field of 20 mT/340 kHz (16 kA m^{-1}). The grey lines represent the best fits with the second-order Taylor series model. Black empty points indicate the magnetothermal experiments for *tert*-butylbenzene alone used as reference, (b) ΔT as a function of the IONP@alkoxyamine nanoparticle concentration.

comparable with those of previously reported IONPs (spherical or cubic ones) permitting the efficient macroscopic magnetothermal heating.[11,12]

To further explore magnetothermal properties of IONP@alkoxyamine nanoparticles, we investigated the influence of the magnetic field strength and solvent nature. First, the experiments were performed at three different amplitudes of AMF (8, 12 and 16 kA m^{-1}) (Fig. S11, ESI†). As expected, the maximal temperature achieved under an application of AMF at 10 min increases with the strength of the magnetic field and no saturation of the heating performance was noted.[12] The calculated SAR values equal to 47, 123 and 205 W g^{-1} (per g of nanoparticles) for the fields of 8, 12 and 16 kA m^{-1}, respectively, follow this tendency. Note that the calculated average ILP value is still equal to 2.4 nHm^2 kg^{-1}, as expected.

Secondly, the solvent's properties, particularly their boiling point, viscosity, and specific heat are important parameters in determining the efficiency of magnetothermal heating.

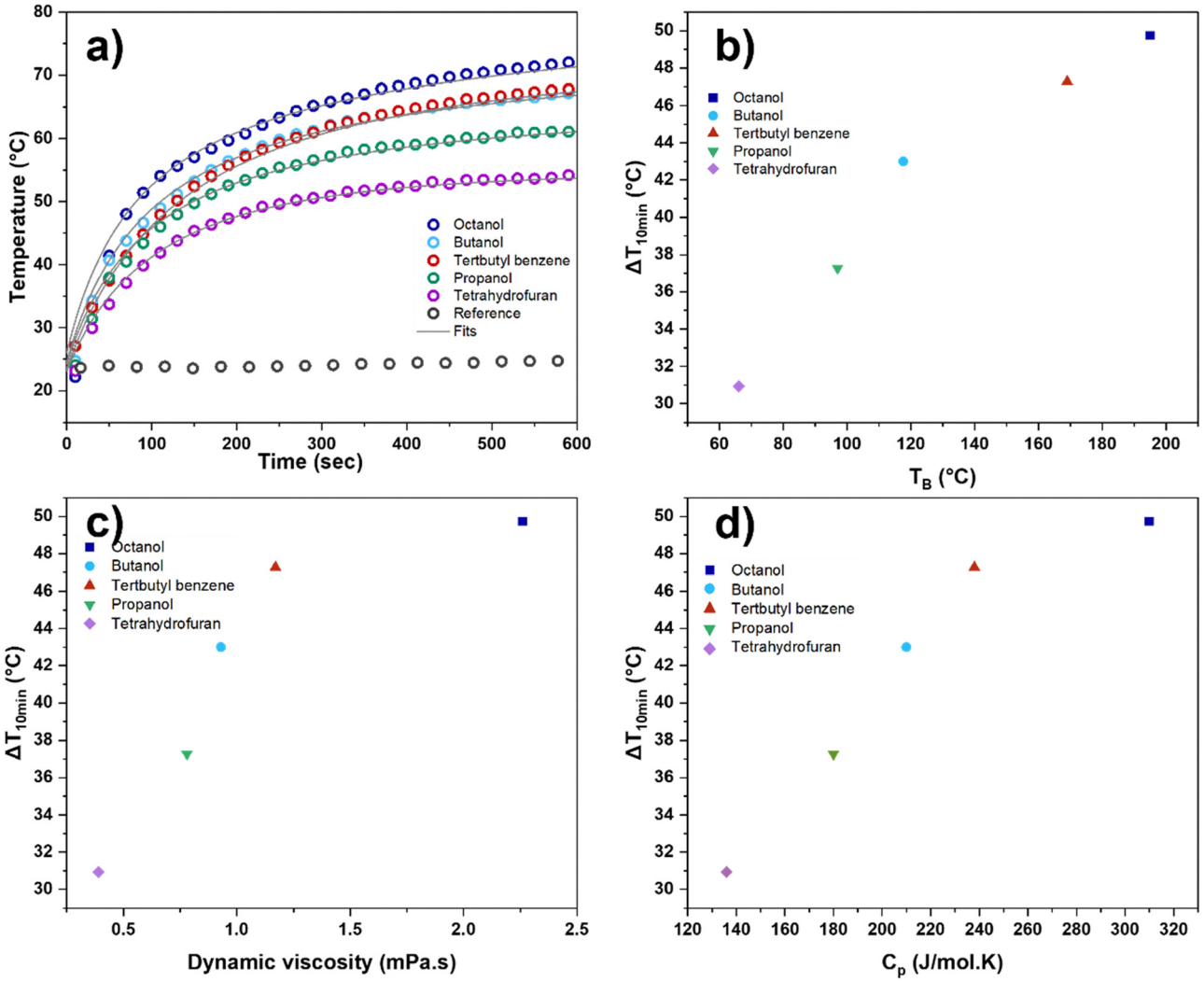

Fig. 4 (a) Magnetothermal experiments performed for IONP@alkoxyamine colloidal solutions with a concentration of 2.9 mg mL^{-1} in different solvents under an applied ac magnetic field of 20 mT/340 kHz. The solid lines represent the best fit with the second-order Taylor series model, (b) Variation of ΔT as a function of boiling temperature of solvent, (c) Variation of ΔT as a function of the solvent viscosity, and (d) Variation of ΔT as a function of the solvent's specific heat (C_p).

Note that, to the best of our knowledge, the influence of solvents on the macroscopic magnetothermal properties was emphasized rather scarcely in the literature.[57] We have primarily assessed the colloidal stability and good dispersibility of our nanoparticles in five selected solvents with varying boiling points and viscosities (octanol, butanol, *tert*-butylbenzene, propanol, and THF), since these factors are crucial for the magnetothermal performance of the nanoparticles.[58,59] DLS analyses (Fig. S12, ESI†) demonstrate that the obtained nanoparticles are rather well dispersed. Then, the magnetothermal heating of five different colloidal solutions of IONP@alkoxyamine (2.9 mg mL^{-1}) in octanol, butanol, *tert*-butylbenzene, propanol and THF was tested with the same AMF strength. Fig. 4 shows that for the same concentration of the nanoparticles, the choice of solvent importantly impacts the macroscopic temperature increase. Fig. 4b–d demonstrates the variation of ΔT as a function of solvent's boiling temperature, dynamic viscosity and specific heat, respectively. As one can see, ΔT increases with the solvent's boiling temperature (Fig. 4b). Note that the measured macroscopic temperature remained below the boiling temperature of the solvents in all cases, even for THF. Indeed, higher boiling point solvents tend to result in a greater temperature increase, as they can sustain higher temperatures without undergoing phase changes, thereby reducing heat dissipation and supporting a higher ΔT. This effect was previously reported by B. Chaudret and coll. in their study of the magnetothermal effect on the catalytic activity of iron carbide nanoparticles.[57] They also highlighted the significant discrepancy between the temperature on the nanoparticle surface and the macroscopic temperature measured in the solution, occurring particularly for solvents with relatively low boiling points. A similar trend is observed for the viscosity of the solvent measured at the maximum temperature reached by the colloidal solution (Fig. 4c). Specifically, ΔT increases as the viscosity

of the solvent increases. This observation rather contrasts with previously published results for magnetic nanoparticles in water and aqueous agar-agar solutions, where magnetothermal heating either decreased or remained unchanged as viscosity of solution increased.[14,60–62] However, the impact of viscosity on magnetothermal heating is rather complex and can vary depending on several factors, including the Brownian relaxation of magnetic nanoparticles, thermal conductivity, the specific heat of the solvent, *etc.* The overall effect of viscosity on magnetothermal heating results from the interplay of these factors. In our case, with different solvents being used, higher viscosity may enhance local heating and reduce heat dissipation, leading to a greater observed temperature increase compared to aqueous solutions. Finally, we plotted ΔT as a function of the solvent's specific heat (C_p of the solvent is measured at the maximal temperature reached in the experiments), which demonstrated that the macroscopic temperature increase is greater with higher C_p (Fig. 4d). Given that the measurements were performed with the same nanoparticles and under identical conditions, with only the solvents differing, this observation is indeed counter-intuitive. However, despite a higher C_p typically requiring more energy to increase the temperature, solvents with a greater C_p can absorb and retain more heat from the nanoparticles. This enhanced heat absorption can result in a more substantial temperature increase in the solvent. Additionally, solvents with higher C_p may experience reduced relative heat loss because they can absorb more heat before a significant temperature increase occurs. This effect can lead to a more pronounced macroscopic temperature increase. Moreover, solvents with higher C_p may facilitate better thermal equilibration within the system, promoting a more even distribution of heat and contributing to a higher overall ΔT. Therefore, the observed impact of the solvent properties (boiling point, viscosity, and specific heat) on magnetothermal heating reveals that macroscopic temperature increase during the AMF action requires careful consideration of the macroscopic environment.

Photothermal properties. Note that investigations into the photothermal properties of IONPs have emerged relatively recently, revealing their ability to efficiently convert near-infrared (NIR) light into heat.[17] Although the precise mechanisms behind this heat generation are not yet fully elucidated, it is known to involve electronic transitions between the valence and conduction bands, with heat produced as electrons return to their original states.[63] Some iron oxide nanoparticles have demonstrated heating capabilities comparable to those of gold nanoparticles, which are considered standard photothermal agents. Moreover, recent studies have shown that certain IONPs can achieve effective photothermal heating at lower concentrations than those typically required for magnetothermia. However, this approach often relies on laser power densities exceeding 1 W cm^{-2}.[64]

The photothermal properties of the IONP@alkoxyamine nanoparticles were investigated under laser irradiation at 808 nm (power 2.6 W cm^{-2}). The macroscopic temperature of the colloidal solutions with the concentrations 0.1–4 mg mL^{-1} under light irradiation was monitored by using an optical fibre

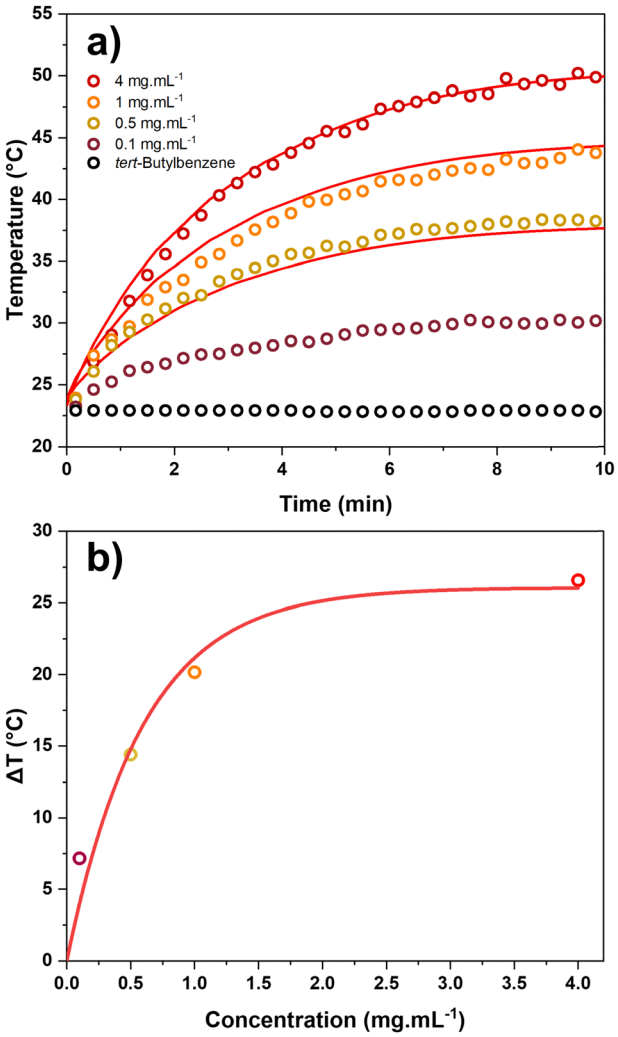

Fig. 5 (a) Temperature profile *vs.* time for IONP@alkoxyamine colloidal solutions with concentrations ranging from 0.1 to 4 mg mL^{-1} in *tert*-butylbenzene obtained under laser irradiation at 808 nm (laser power of 2.6 W cm^{-2}). Solid line represents the fit of the curves with the COMSOL program. (b) Corresponding ΔT *vs.* IONP@alkoxyamine nanoparticle concentration dependence. The red curve represents the fit obtained using eqn (S19) (ESI†).

introduced in solution. A macroscopic heating of *tert*-butylbenzene colloidal solutions was observed after a few minutes of irradiation in the presence of nanoparticles, while the nanoparticle-free *tert*-butylbenzene remains unheated (Fig. 5a). The temperature profiles for investigated concentrations (0.1–4 mg mL^{-1}) were drawn for 10 min of irradiation. Fig. 5b shows ΔT which first increases quasi linearly at low concentration (below 1 mg mL^{-1}). Then, at 4 mg mL^{-1} a plateau is reached. This well-known effect in the literature can be explained by the limitation of the penetration depth of the laser in the sample due to the optical saturation, limited interaction sites, and self-screening and quenching effects.[65,66] Note that, in contrast, magnetothermal heating (Fig. 3) acts as a volumetric process, where the entire nanoparticle population contributes to heat generation. This mechanism is not limited by the optical

penetration depth, resulting in a more pronounced difference in the temperature increase as a function of concentration in the AMF experiments (ΔT until 50 °C at 4 mg mL). In the ESI,† a model was developed to describe the shape of ΔT as a function of the concentration curve. Eqn (S19) (see Models and the theory part in the ESI†) describes the evolution of ΔT, which depends exponentially on the thickness of the sample and the concentration of the substance in question. The light-to-heat conversion efficiency (η), which is the conventional parameter employed for the comparison of different photothermal agents, was calculated by fitting the T *vs.* time curves at low concentrations with the COMSOL program (see the Experimental part for details and Fig. 5). The obtained η value of 30 ± 1% is among the highest previously reported values for different IONPs.[18]

Kinetics of radical release

The controlled radical release in a multistep way was investigated by using EPR spectroscopy for: (i) free alkoxyamine molecules upon thermal heating in order to determine their activation energy (E_a) and half-life time, (ii) IONP@alkoxyamine nanoparticles under applied AMF, and (iii) IONP@alkoxyamine nanoparticles under laser irradiation at 808 nm.

First, the homolysis reaction of *tert*-butylbenzene solution of the free (6-(4-(1-((di-*tert*-butylamino)oxy)ethyl)benzamido)hexyl) phosphonic acid (10^{-4} M) was investigated at three different temperatures, 44, 65 and 77 °C, by using EPR spectroscopy (by taking aliquots and analysing them by EPR) (Fig. 6a). Note that the EPR spectrum of this molecule is silent before thermal activation, while upon heating it shows a three line profile corresponding to the nitroxide (I_N = 1, S = 1/2) generated by the homolysis of the thermosensitive C–ON bond (Fig. 6b).[43] The hyperfine coupling constant is equal to 15.6 G, which is in agreement with previously reported results on nitroxide. This clearly indicates that the free alkoxyamine is stable at room temperature and delivers radicals only upon heating. The kinetics of the radical delivery for three investigated temperatures represented as the C/C_0 *vs.* heating time curve (up to 2.5 h) (Fig. 6c) was fitted with (eqn (1)):

$$[\mathrm{rad}] = [\mathrm{rad}]_\infty(1 - \mathrm{e}^{-k_d t}), \quad (1)$$

which is the analytical solution of the following kinetic differential equations:

$$\frac{\mathrm{d}[\mathrm{alkox}]}{\mathrm{d}t} = -k_\mathrm{d}[\mathrm{alkox}] \quad (2)$$

and

$$\frac{\mathrm{d}[\mathrm{rad}]}{\mathrm{d}t} = k_\mathrm{d}[\mathrm{alkox}], \quad (3)$$

where k_d is the rate homolysis constant, t is the time, [rad] is the concentration of the generated nitroxide during homolysis, and $[\mathrm{rad}]_\infty$ stands for the concentration of nitroxide when the plateau is reached, *i.e.*, $[\mathrm{rad}]_\infty = [\mathrm{alkox}]_0$ = 0.1 mM. Then, the Arrhenius law, as set forth in eqn (4), permits us to provide

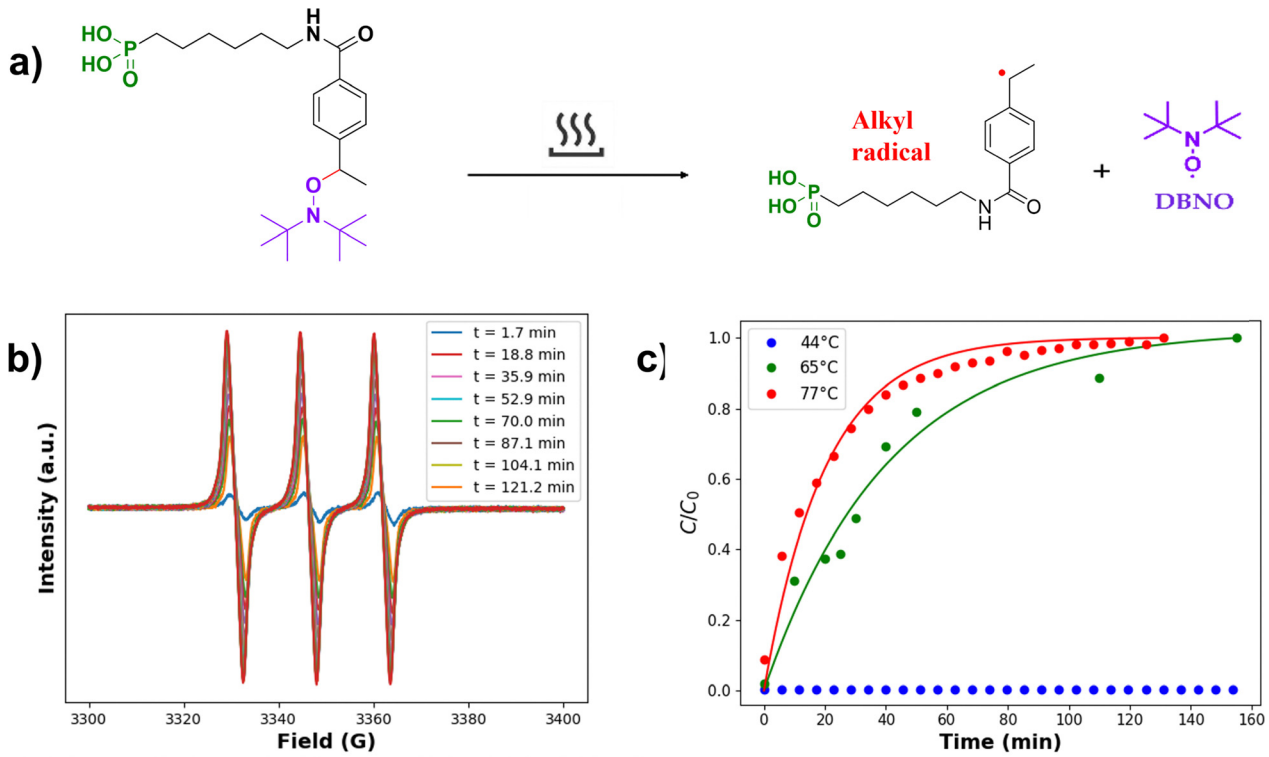

Fig. 6 (a) Schematic representation of the (6-(4-(1-((di-*tert*-butylamino)oxy)ethyl)benzamido)hexyl) phosphonic acid alkoxyamine homolysis upon heating; (b) representative EPR spectra performed for the (6-(4-(1-((di-*tert*-butylamino)oxy)ethyl)benzamido)hexyl) phosphonic acid alkoxyamine before and afer heating at 77 °C during different periods of time; and (c) C/C_0 *vs.* time curve obtained for alkoxyamine under three different heating temperatures: 44, 65, at 77 °C. Solid line represents the best fits to the data with eqn (1).

the activation energy of the alkoxyamine's homolysis, E_a, and its half-life time, $t_{1/2}$: From (eqn 1),

$$E_a = -RT \ln\left(\frac{k_d}{A}\right) \quad (4)$$

the half-life time, $t_{1/2}$, has been determined as $t_{1/2} = (\ln 2)/k_d$.

The employment of these equations allowed us to obtain the following parameters (for both temperatures): $k_d = 6.4 \times 10^{-4}$ s^{-1} at 77 °C (100% conversion), $E_a = 117.8$ kJ mol^{-1} and $t_{1/2} = 33$ days at 20 °C. The average pre-exponential factor $A = 2.4 \times 10^{14}$ s^{-1} has been fixed for this fit as previously reported.[67] Note that the obtained activation energy is significantly lower (and at lower temperature) in comparison with that previously published by us (6-{4-[1-(2,2,6,6-tetramethyl-piperidin-1-yloxy)-ethyl]-benzoyl-amino}-hexyl)-phosphonic acid alkoxyamine used for a similar purpose, for which we found the following parameters $k_d = 7.0 \times 10^{-4}$ s^{-1} at 115 °C (91% conversion), $E_a = 130.3$ kJ mol^{-1} and $t_{1/2} = 15.6$ years at 20 °C.[48] This signifies that the homolysis of our new alkoxyamine can be produced at lower temperature compared to the previously investigated (6-{4-[1-(2,2,6,6-tetramethyl-piperidin-1-yloxy)-ethyl]-benzoylamino}-hexyl)-phosphonic acid or at the same temperature, but much more rapidly. As an example, $t_{1/2}$ for our new alkoxyamine is equal to 18 min, 1 h 18 min and 20 h at 77, 65 and 44 °C, respectively.

Second, the radical formation for IONP@alkoxyamine nanoparticles was investigated in 2.9 mg mL^{-1} of *tert*-butylbenzene

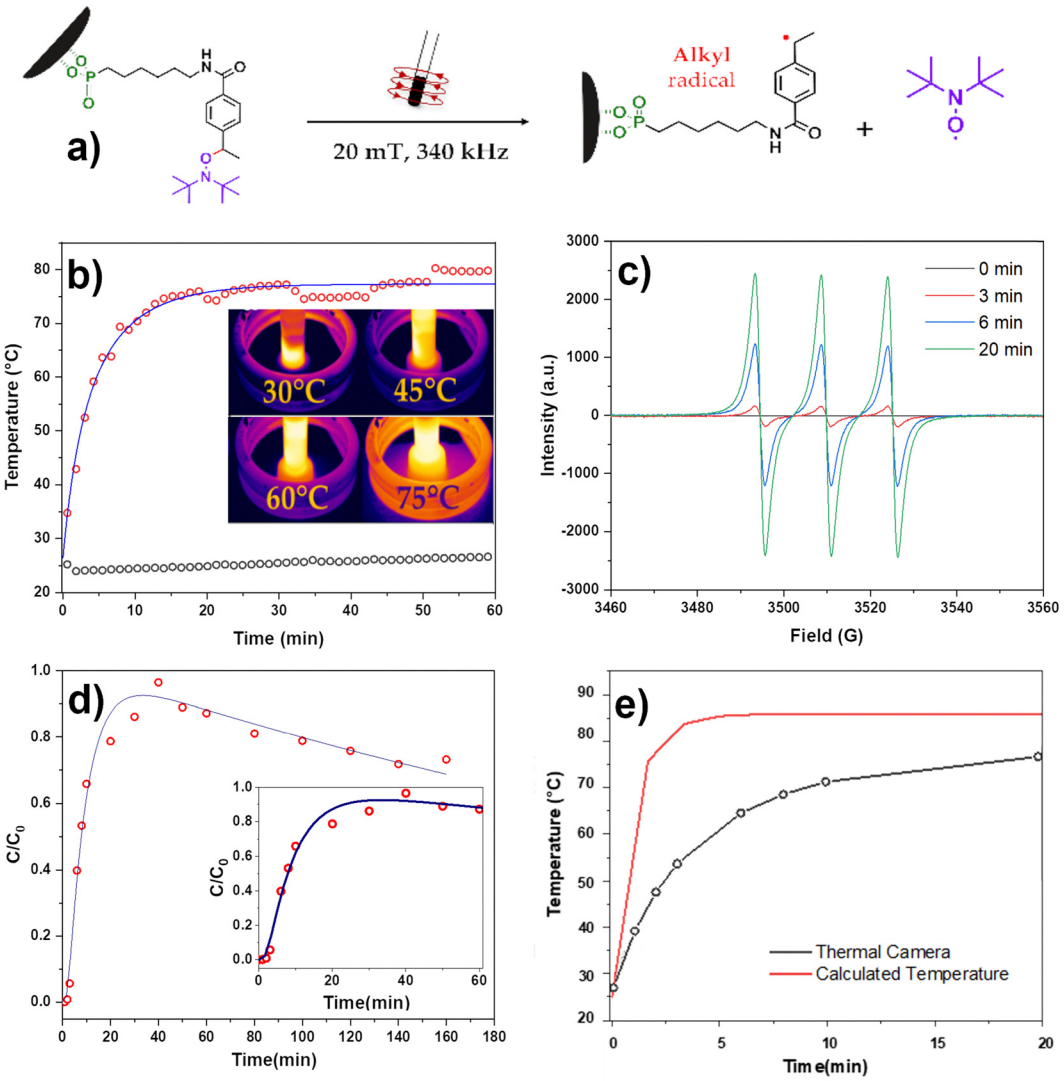

Fig. 7 (a) Schematic representation of the alkoxyamine homolysis in IONP@alkoxyamine nanoparticles under AMF; (b) temperature as a function of time curve for IONP@alkoxyamine nanoparticles (2.9 mg mL^{-1}) exposed to AMF (340 kHz and 20 mT) (red circles) and *tert*-butylbenzene without nanoparticles taken as reference (grey circles). Solid line represents the best fit of the curve with the second-order Taylor series model. Inset: thermal images recorded by a thermal camera during this experiment, (c) EPR spectra for the colloidal solution of IONP@alkoxyamine (2.9 mg mL^{-1}) at different times of exposure to AMF (340 kHz and 20 mT); (d) homolysis kinetics represented as the C/C_0 *vs.* time curve for IONP@alkoxyamine (2.9 mg mL^{-1}) at different times of AMF exposure (340 kHz and 20 mT). Solid line represents the best fit with eqn (5) and (6). Inset: magnification of the curve in the 0–60 min intervale of time; and (e) evaluation of measured macroscopic temperature (black curve) and determined homolysis temperature (red curve) as a function of time during magnetothermal heating of IONP@alkoxyamine nanoparticles.

colloidal solution upon exposure under an action of AMF of 340 kHz and 20 mT (Fig. 7a). The choice of *tert*-butylbenzene as a solvent has been motivated by its high boiling point (169 °C), optimal magnetothermal heating (Fig. 4) and colloidal stability of nanoparticles (Fig. S12, ESI†). Fig. 7b shows the macroscopic temperature elevation during the magnetothermal heating of this colloidal solution for 60 min. The temperature increases quickly during the first 12 min, then more gradually and stabilizes at 77 °C for the remainder of the period. To quantify the quantity of radicals formed over time, aliquots were taken from the colloidal solution at precise time intervals. To analyse the presence of radicals by EPR, the magnetic nanoparticles were removed from the samples using a 5 T magnet. The EPR spectra of the samples taken before the application of the magnetic field and the ones at 3, 6 and 20 minutes after magnetothermal heating are shown in Fig. 7c. As expected, the EPR spectrum is silent before the application of the magnetic field, indicating that the IONP@alkoxyamine nanoparticles are stable at room temperature, with no radicals formed in the absence of an external stimulus. Following the application of AMF, the spectra display three characteristic lines (a hyperfine coupling constant of 15.6 G) with increasing intensities over time, indicating a growing quantity of released radicals. The homolysis kinetics is represented here as the time dependence of the normalized concentration, C/C_0, shown in Fig. 7d. The concentration of radicals increases very rapidly during the first 20 min due to efficient C–ON bond homolysis induced by localized heating on the nanoparticle surface triggered by the action of the AMF. At this time, the macroscopic temperature of the colloidal solution reaches 77 °C, with the homolysis rate (alkoxyamine conversion rate) determined to be 94%. After this, the curve begins to decrease due to the recombination and degradation of the formed radicals. This result successfully demonstrated that the IONP@alkoxyamine nanoparticles generate radicals efficiently under magnetothermal heating. In comparison with the previously published studies on IONP nanoparticles grafted with (6-{4-[1-(2,2,6,6-tetramethyl-piperidin-1-yloxy)-ethyl]-benzoylamino}-hexyl)-phosphonate alkoxyamine, which delivered 70% of radicals after 100 minutes of exposure to AMF,[48] the current system exhibits nearly complete homolysis (94%) after just 20 min of exposure demonstrating therefore superior performance.

Since the thermosensitive alkoxyamines are directly attached to the surface of the nanoparticles, their homolysis reaction can be used to estimate the surface temperature of the nanoparticles. Fig. 7d demonstrates a bell-shaped curve for the C/C_0 *vs.* time dependence. As previously stated, this behaviour can be attributed to a recombination of the radical. For this purpose, the previous model described by eqn (2) and (3) is replaced by the following theoretical model to fit the C/C_0 *vs.* time curve. The evolution of the radical concentration over time can be expressed using the coupled eqn (5) and (6):

$$\frac{\mathrm{d[alkox]}}{\mathrm{d}t} = -k_\mathrm{d}[\mathrm{alkox}] \tag{5}$$

$$\frac{\mathrm{d[rad]}}{\mathrm{d}t} = k_\mathrm{d}[\mathrm{alkox}] - k_1[\mathrm{rad}]. \tag{6}$$

The initial equation serves to model the kinetic chemical reaction, whereby radicals are produced from alkoxyamine grafted to the surface of IONPs, governed by the homolysis rate constant, k_d. The second equation describes the temporal evolution of the concentration of radicals produced and recombined/degraded, where k_1 is the recombination/degradation constant. Note that we assumed the recombination of radicals follows a pseudo-first-order reaction for simplicity. The k_d constant follows the Arrhenius law:

$$k_\mathrm{d} = A \times \exp(-E_\mathrm{a}/RT(t)), \tag{7}$$

where the values of the pre-exponential factor A and the energy barrier E_a were fixed for the free alkoxyamine molecule's homolysis. In this equation, the $T(t)$ term represents the variation of the temperature on the surface of the nanoparticles as a function of time. For simplicity, it was assumed that the temperature on the nanoparticle surface follows Newton's law of cooling. It can be expressed by eqn (8):

$$T(t) = (T_\mathrm{max} - T_0)(1 - \exp(-t/\tau_\mathrm{T})) + T_0 \tag{8}$$

where T_0 is the initial temperature (room temperature), T_max is the maximal temperature and τ_T is the heating rate. Theoretical curves were obtained through the numerical solution of eqn (5) and (6), in conjunction with the utilisation of eqn (7) and (8).

The best fit of the experimental C/C_0 *vs.* time curve with this equation afforded the following parameters: $T_\mathrm{max} = 86 \pm 1$ °C, $k_1 = (4.2 \pm 0.3) \times 10^{-5}$ s^{-1}, and $\tau_\mathrm{T} = 59 \pm 13$ s. This result indicates that the maximum temperature for complete homolysis, as determined by fitting, is higher than the macroscopic temperature measured by the optical fibre or thermal camera. Variations of the homolysis rate constant as a function of temperature and time are provided in Fig. S13a and b (ESI†). Therefore, by using eqn (8), we were able to plot the homolysis temperature as a function of time. This temperature corresponds to the region close to the nanoparticles' surface (approximately 15–20 Å from the surface). Fig. 7e compares the macroscopic temperature of the colloidal solution with the estimated homolysis temperature, highlighting a substantial discrepancy. The homolysis temperature increases rapidly to 86 °C within 2.5 minutes and then stabilizes, whereas the macroscopic temperature only reaches 77 °C after 12 minutes. This discrepancy could be explained by two hypotheses:

(i) The presence of a localised heating within the thin corona, just in a few nanometers around the nanoparticles, could result in a temperature significantly higher than that in the bulk solution. The rapid increase and stabilization of the homolysis temperature near the nanoparticles suggest that these nanoscale regions experience more intense thermal conditions than the bulk solution. After 12 minutes, ΔT between the surface and bulk solution temperatures was measured at 9 °C, in good agreement with our previous experiments.[48] Although still a topic of debate, the existence of a ''hot spot''

effect in IONPs subjected to AMF has been previously proposed under certain conditions in the literature.[10,68–72]

(ii) Alternatively, a catalytic effect under AMF could be accelerating the homolysis reaction specifically on the surface of the alkoxyamine-grafted nanoparticles, enhancing the reaction rate locally and independently of the overall solution temperature. Some catalytic effects under magnetic field application, including AMF, have indeed been reported in the literature.[73] Note also that compared to the free alkoxyamine (6-(4-(1-((di-*tert*-butylamino)oxy)ethyl)benzamido)hexyl)phosphonic acid heated at 77 °C, AMF exposure accelerates the homolysis of alkoxyamine-grafted nanoparticles (16 kA m^{-1}, 2.9 mg mL^{-1}) twofold ($t_{1/2}$ = 7.9 min for IONP@alkoxyamine *vs.* 18 min for alkoxyamine). Moreover, almost 1 h required for $t_{1/2}$ conversion in our earlier IONP grafted with (6-{4-[1-(2,2,6,6-tetramethylpiperidin-1-yloxy)-ethyl]benzoylamino}-hexyl)-phosphonate alkoxyamine nanoparticles at a higher temperature (110 °C).[48]

Third, the radical formation was also investigated under laser irradiation (photothermal heating). For this, the colloidal solution of the IONP@alkoxyamine nanoparticles of the concentration of 1 mg mL^{-1} was continually irradiated at 808 nm at a power of 2.6 W cm^{-2} for 10, 20 and 60 min. Note that, unlike in radical release experiments under magnetothermal heating using a nanoparticle concentration of 2.9 mg mL^{-1}, we initially selected an optimal concentration of 1 mg mL^{-1} to avoid optical saturation effects (Fig. 5). For each time, the magnetic nanoparticles were separated by magnetic decantation, and the remaining supernatants were analysed by EPR to quantify the radical release. The EPR spectrum is silent before irradiation, indicating that no radicals were present in the initial solution. However, after 10 minutes of irradiation, three characteristic lines appear in the EPR spectrum, signalling the presence of radicals (Fig. 8a). The intensity of these lines increases with continued irradiation. The nitrogen hyperfine coupling constant is equal to 15.6 G. The C/C_0 *vs.* time curve for photothermal activation of homolysis shown in Fig. 8b reveals that a half conversion ($t_{1/2}$) is achieved after 23.6 min at 44 °C, while the free molecule requires 20 h to reach the same conversion at this temperature. This finding demonstrates that radical production can be achieved through photothermal activation at temperatures not exceeding 44 °C (see Fig. 5a for temperature measurements during photothermal heating). Note also that the continuous irradiation of the free alkoxyamine molecule under the same conditions (808 nm, 2.6 W cm^{-2}, *tert*-butylbenzene) did not give the appearance of clear radical's signal in the EPR spectrum (Fig. S14, ESI†). A similar experiment was performed at the same nanoparticles' concentration of 2.9 mg mL^{-1} as used in the magnetothermal studies, allowing for a comparison between magnetothermal and photothermal effects (Fig. S15, ESI†). In this case, a half-conversion time of $t_{1/2}$ = 12.7 min was observed.

Eqn (2) and (3), as well as the macroscopic temperature (T) monitored during the experiments were used to fit the C/C_0 *vs.* time curves to obtain the real homolysis temperature in the vicinity of the nanoparticles surface ($T + \Delta T$) (solid line in Fig. 8b and Fig. S15, ESI†). For a nanoparticle concentration of

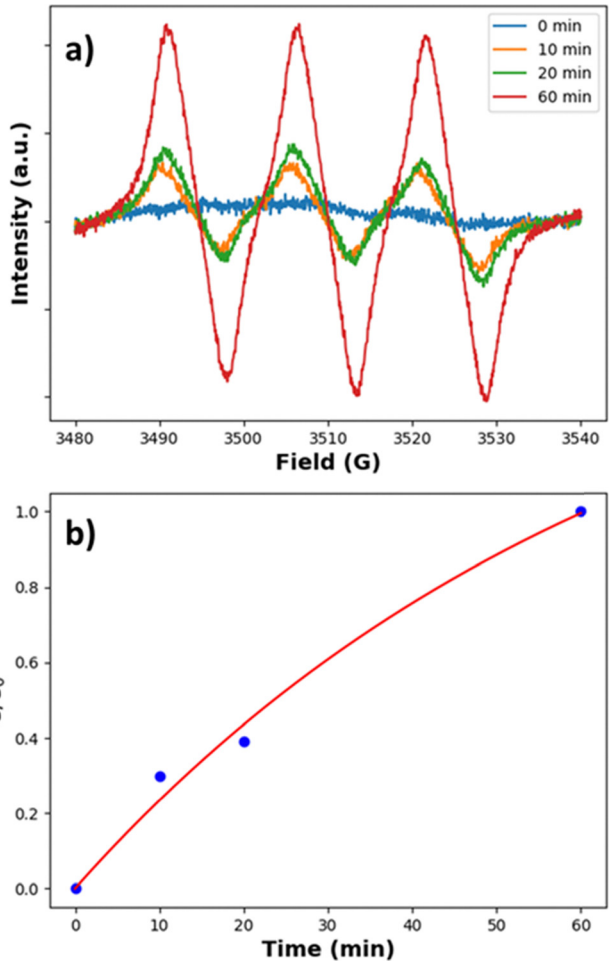

Fig. 8 (a) EPR spectra of the *tert*-butylbenzene solutions of IONP@alkoxyamine (1 mg mL^{-1}) before and after 10, 20 and 40 min after light irradiation at 808 nm (2.6 W cm^{-2}); (b) homolysis kinetics represented as the C/C_0 *vs.* time curve. The red line represents the best fit with eqn (2) and (3).

1 mg mL^{-1}, the following parameters were obtained: T_{max} = 107 ± 5 °C, k_d = 1.5 × 10^{-2} s^{-1}. Notably, a very significant discrepancy (ΔT) of 63 °C was observed between the measured macroscopic temperature of the solution (44 °C) and the temperature near the nanoparticle surfaces (107 °C). Comparable results were obtained for the photothermal experiment performed at a concentration of 2.9 mg mL^{-1}, with a discrepancy ΔT = 59 °C between macroscopic and local temperatures. This pronounced difference suggests that the alkoxyamine homolysis occurring at the nanoparticle surface under light irradiation is considerably more intense than what would be expected based on the bulk solution heating alone. This phenomenon also observed under AMF, though it appears to be even more pronounced in the case of photothermal activation. To explain this discrepancy, two hypotheses should also be considered. Firstly, the intense local heating observed in photothermal experiments could result from a localized photothermal effect, leading to more concentrated heating than magnetothermal activation due to distinct mechanisms of heat

generation and dissipation. Secondly, an autocatalytic homolysis effect under light irradiation may also be influencing the process, particularly for alkoxyamines grafted onto the nanoparticle surface. For instance, thermosensitive alkoxyamine derivatives covalently attached to spherical Au nanoparticles *via* pendant $-NH_2$ groups have shown the capacity to generate radicals through plasmonic activation by light irradiation without heating of the bulk solution.[74] Notably, in the absence of IONPs, the alkoxyamine alone did not produce radicals under identical irradiation conditions.

These results highlight the critical importance of localized nanoscale effects, demonstrating that the alkoxyamine's homolysis rate on the nanoparticle surface subjected to the action of external stimuli is significantly elevated compared to consideration of only a bulk solution heating. This enhancement is even much more pronounced under light irradiation. Further investigation is required to determine the primary factors driving alkoxyamine homolysis in this context. Moreover, the comparison between AMF and photothermal heating showed that after 20 min of AMF exposure, homolysis conversion reached 94%, whereas NIR photothermal experiments yielded 39.1% conversion at 1 mg mL^{-1} and 75% at 2.9 mg mL^{-1}. This difference is primarily due to the distinct macroscopic temperatures achieved: magnetothermal heating reached 77 °C, while photothermal heating produced lower macroscopic temperatures (44 °C at 1mg mL^{-1} and 50 °C at 2.9 mg mL^{-1}) due to the intrinsic optical limitations and saturation effects of the NIR approach. However, as highlighted above, factors beyond macroscopic temperature, such as elevated local temperatures at the nanoparticle surface and/or autocatalytic effects, can influence radical release.

Experimental part

Materials

All chemical reagents were purchased from commercial suppliers (Sigma-Aldrich, Sikémia, and TCI) and used without further purification. Ferric hydroxide oxide (FeO(OH) hydrated, 30–50 mesh), oleic acid (90%) and oleylamine (90%) were obtained from Sigma Aldrich; *n*-docosane (99%) was obtained from Acros organic. Pentane, diethyl ether, cyclohexane, acetone and ethanol were purchased from Merck. All organic chemistry experiments were performed under anhydrous conditions and an inert atmosphere of argon and, except where stated, using dried apparatus, and employing standard techniques for handling air-sensitive materials. Routine reaction monitoring was performed using silica gel 60 F254 TLC plates; the spots were visualized upon exposure to UV light and a *p*-anisaldehyde or phosphomolybdic acid solution in EtOH followed by heating. Purifications were performed on chromatography columns with silica gel grade 60 (230–400 mesh).

Syntheses

Syntheses of the DBNO alkoxyamine derivative

Methyl 4-vinylbenzoate. A solution of 4-vinylbenzoic acid (5.00 g, 33.8 mmol, 1 eq.) and K_2CO_3 (45.8 g, 331 mmol, 9.8 eq.) was stirred under argon, at room temperature. Then, iodomethane (2.50 mL, 40.5 mmol, 1.2 eq.) was added slowly. The reaction was controlled by TLC (DCM/MeOH 95 : 5). After the reaction, water was added to the reaction mixture, and the reaction mixture was extracted with Et_2O. The organic layer was washed with water and dried on $MgSO_4$, and the solvent was removed under vacuum. The crude was purified by column chromatography (DCM/MeOH gradient from 0% to 5% of MeOH) to yield methyl-4-vinylbenzoate quantitatively. The ^1H spectra of this compound were identical to the one reported. ^{11}H NMR (300 MHz, $CDCl_3$): δ 8.10–7.89 (m, 2H, $H_{(2,4)}$), 7.52–7.39 (m, 2H, $H_{(1,5)}$), 6.75 (dd, J = 17.6, 10.9 Hz, 1H, $H_{(7)}$), 5.86 (dd, J = 17.6, 0.5 Hz, 1H, $H_{(8Z)}$), 5.38 (d, J = 10.9 Hz, 1H, $H_{(8E)}$), 3.91 (s, 3H, $H_{(10)}$).

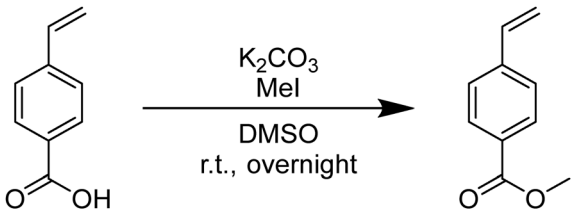

Methyl 4-(1-((di-tert-butylamino)oxy)ethyl)benzoate. In an open-air flask, methyl 4-(1-((di-*tert*-butylamino)oxy)ethyl) benzoate and $MnCl_2$ (73 mg, 0.37 mmol, 0.1 eq.) were added to a stirred solution of the salen ligand (99 mg, 0.37 mmol, 0.1 eq.) in THF. After 30 minutes of stirring at room temperature, a solution of the di-*tert*-butyl-nitroxide (DBNO) radical (0.81 g, 5.55 mmol, 1.5 eq.) and methyl 4-vinylbenzoate (0.60 g, 3.70 mmol, 1 eq.) in THF was added, then, $NaBH_4$ powder (4 eq.) was added in small portion. The resulting suspension was stirred at room temperature for 24 h. It was then diluted with EtOAc and 1 M aq. HCl was carefully added up to pH ~ 1–2. Solid $NaHCO_3$ was then added until neutralization. The layers were separated, and the organic phase was washed with water, then brine and dried over $MgSO_4$. After concentrating under reduced pressure, the residue was purified by column chromatography (EP/Et_2O gradient from 0% to 6% of Et_2O) to yield methyl 4-(1-((di-*tert*-butylamino)oxy)ethyl)benzoate (0.83 g, 73%). ^1H NMR (400 MHz, $CDCl_3$): δ 8.01–7.97 (m, 2H, $H_{(2,4)}$), 7.42–7.37 (m, 2H, $H_{(1,5)}$), 4.88 (q, J = 6.7 Hz, 1H, $H_{(7)}$), 3.91 (s, 3H, $H_{(10)}$), 1.49 (d, J = 6.7 Hz, 3H, $H_{(8)}$), 1.32 (s, 3 × CH_3, $H_{(14)}$), 1.03 (s, 3 × CH_3, $H_{(13)}$). ^{13}C NMR (101 MHz, $CDCl_3$): δ 167.1 (CO, $C_{(9)}$), 150.7 (Cq, $C_{(6)}$), 129.4 (2 × CH, $C_{(2,4)}$), 128.6 (Cq, $C_{(3)}$), 126.6 (2 × CH, $C_{(1,5)}$), 82,7 (CH, $C_{(7)}$), 62.0 (Cq, $C_{(11)}$), 61.8 (Cq, $C_{(12)}$), 51.9 (CH_3, $C_{(10)}$), 30.7 (3 × CH_3, $C_{(13)}$), 30.6 (3 × CH_3, $C_{(14)}$), 22.8 (CH_3, $C_{(8)}$). HRMS (ESI): calc. $[M + H]^+$: 308.2220; found: 308.2218.

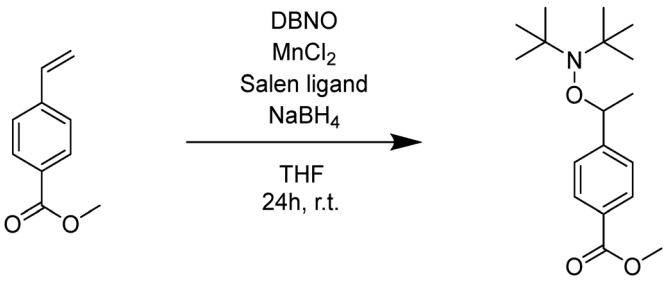

4-(1-((Di-tert-butylamino)oxy)ethyl)benzoic acid. KOH (0.84 g, 15 mmol, 8 eq.) was added to a solution of the ester-based alkoxyamine (0.95 g, 2.98 mmol, 1 eq.) in THF–H_2O–MeOH (1 : 1 : 1) at room temperature. The mixture was stirred for 6 h and then acidified with 1 M HCl. The mixture was diluted with water and extracted with DCM. The combined organic phase was dried on $MgSO_4$ and the solvent was evaporated. The crude was purified by column chromatography (DCM:MeOH gradient from 0% to 5% of MeOH) to afford 4-(1-((di-*tert*-butylamino)-oxy)ethyl)benzoic acid in 92% yield (840 mg). ^{1}H NMR (300 MHz, $CDCl_3$): δ 9.96 (br s, 1H, COOH), 8.95–7.85 (m, 2H, $H_{(2,4)}$), 7.30–7.22 (m, 2H, $H_{(1,5)}$), 4.74 (br q, J = 5.5 Hz, 1H, $H_{(7)}$), 1.33 (br d, J = 5.4 Hz, 3H, $H_{(8)}$) 1.15 (s, 3 × CH_3, $H_{(13)}$), 0.87 (s, 3 × CH_3, $H_{(14)}$). ^{13}C NMR (75 MHz, $CDCl_3$): δ 172.1 (CO, $C_{(9)}$), 151.8 (Cq, $C_{(6)}$), 130.3 (2 × CH, $C_{(2,4)}$), 128.1 (Cq, $C_{(3)}$), 126.7 (2 × CH, $C_{(1,5)}$), 82.9 (CH, $C_{(7)}$), 62.4 (Cq, $C_{(11)}$), 62.1 (Cq, $C_{(12)}$), 30.8 (3 × CH_3, $C_{(13)}$), 30.2 (3 × CH_3, $C_{(14)}$), 23.7 (CH_3, $C_{(8)}$). HRMS (ESI): calcd $[M + H]^+$: 294.2064; found: 294.2060.

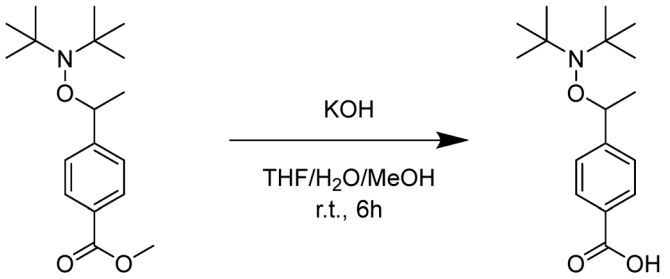

Diethyl(6-(4-(1-((di-tert-butylamino)oxy)ethyl)benzamido) hexyl)phosphonate. DMAP (47 mg, 0.39 mmol, 0.3 eq.) was added to a stirred solution of alkoxyamine (500 mg, 1.63 mmol, 1 eq.) in DCM (5 mL) and the solution was stirred at room temperature under argon for 10 min. After the addition of EDCI (0.38 g, 2.45 mmol, 1.5 eq.), the solution was stirred at room temperature for a further 30 min, then, amine (503 mg, 2.12 mmol, 1.3 eq.) was added at 0 °C. The reaction mixture was stirred at room temperature overnight. The mixture was washed with 1 M HCl, $NaHCO_3$ (saturated solution), distilled water, and brine. The organic phase was dried with $MgSO_4$, and the solvent was removed under vacuum. The purification by column chromatography (DCM/MeOH from 0% to 6% of MeOH) yielded diethyl(6-(4-(1-((di-*tert*-butylamino)oxy)ethyl) benzamido)hexyl)-phosphonate (0.835 g, 99%). ^{1}H NMR (300 MHz, $CDCl_3$): δ 7.71–7.65 (m, 2H, $H_{(2,4)}$), 7.27–7.22 (m, 2H, $H_{(1,5)}$), 6.80 (t, J = 5.5 Hz, 1H, NH), 4.76 (q, J = 6.7 Hz, 1H, $H_{(7)}$), 4.04–3.90 (m, 4H, $H_{(21)}$), 3.32 (dd, J = 12.9, 6.8 Hz, 2H, $H_{(15)}$), 1.38 (d, J = 6.7 Hz, 3H, $H_{(8)}$), 1.21 (t, J = 7.1 Hz, 2 × CH_3, $H_{(22)}$), 1.21 (s, 3 × CH_3, $H_{(13)}$), 1.70–1.15 (m, 10H, $H_{(16,17,18,19,20)}$), 0.93 (s, 3 × CH_3, $H_{(14)}$). ^{13}C NMR (75 MHz, $CDCl_3$): δ 167.4 (CO, $C_{(9)}$), 148.7 (Cq, $C_{(6)}$), 133.2 (Cq, $C_{(3)}$), 126.8 (2 × CH, $C_{(2,4)}$), 126.7 (2 × CH, $C_{(1,5)}$), 82.6 (CH, $C_{(7)}$), 61.9 (Cq, $C_{(11)}$), 61.7 (Cq, $C_{(12)}$), 61.3 (d, J_{C-P} = 6.5 Hz, 2 × CH_2, $C_{(21)}$), 39.7 (CH_2, $C_{(15)}$), 30.63 (3 × CH_3, $C_{(13)}$), 30.58 (3 × CH_3, $C_{(14)}$), 30.0 (d, J_{C-P} = 16.3 Hz, CH_2, $C_{(19)}$), 29.3 (CH_2, $C_{(16)}$), 26.3 (CH_2, $C_{(17)}$), 25.4 (d, J_{C-P} = 140.4 Hz, CH_2, $C_{(20)}$), 22.8 (CH_3, $C_{(8)}$), 22.2 (d, J_{C-P} = 5.1 Hz, CH_2, $C_{(18)}$), 16.4 (d, J_{C-P} = 6.0 Hz, 2 × CH_3, $C_{(22)}$). ^{31}P NMR (162 MHz, $CDCl_3$): δ 32.26. HRMS (ESI): calcd $[M + H]^+$: 513.3452; found: 513.3452.

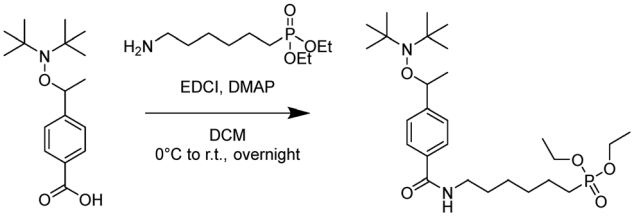

(6-(4-(1-((Di-tert-butylamino)oxy)ethyl)benzamido)hexyl) phosphonic acid. The phosphonate-based alkoxyamine (835 mg, 1.63 mmol, 1 eq.) was dissolved in DCM (25 mL) and cooled at −20 °C. Then, TMSBr (780 µL, 3.5 eq.) was added and the reaction was stirred for 3 h at room temperature. The solvent was evaporated under reduced pressure and the residual mixture was dissolved in methanol (20 mL) and stirred for 30 min. The solvent was evaporated under reduced pressure to yield (6-(4-(1-((di-*tert*-butylamino)oxy)ethyl)benzamido)hexyl)phosphonic acid as a white powder, which was pure enough to be used without further purification. (743 mg, quantitative). ^{1}H NMR (300 MHz, MeOD): δ 7.87–7.83 (m, 2H, $H_{(2,4)}$), 7.58–7.54 (m, 2H, $H_{(1,5)}$), 5.84 (q, J = 6.4 Hz, 1H, $H_{(7)}$), 3.36 (t, J = 7.1 Hz, 2H, $H_{(15)}$), 1.35–1.76 (m, 5 × CH_2, $H_{(16,17,18,19,20)}$), 1.72 (d overlapped, J = 6.4 Hz, 3H, $H_{(8)}$), 1.73 (s, 3 × CH_3, $H_{(13)}$), 1.40 (s, 9H, $H_{(14)}$); ^{13}C NMR (75 MHz, MeOD): δ 169.3 (CO, $C_{(9)}$), 145.4 (Cq, $C_{(6)}$), 136.0 (Cq, $C_{(3)}$), 128.9 (2 × CH, $C_{(2,4)}$), 127.9 (2 × CH, $C_{(1,5)}$), 87.9 (CH, $C_{(7)}$), 77,4 (Cq, $C_{(11)}$), 77.0 (Cq, $C_{(12)}$), 40.9 (CH_2, $C_{(15)}$), 31.2 (d, J_{C-P} = 16.5 Hz, CH_2, $C_{(19)}$), 30.2 (CH_2, $C_{(16)}$), 28.64 (3 × CH_3, $C_{(13)}$), 28.62 (3 × CH_3, $C_{(14)}$), 27.8 (d, J_{C-P} = 137.1 Hz, CH_2, $C_{(20)}$), 26.9 (CH_2, $C_{(17)}$), 24.4 (CH_3, $C_{(8)}$), 23.70 (d, J_{C-P} = 5.0 Hz, CH_2, $C_{(18)}$); ^{31}P NMR (121 MHz, MeOD): δ 30.11; HRMS (ESI) calcd $[M + H]^+$: 457.2826; found: 457.2827.

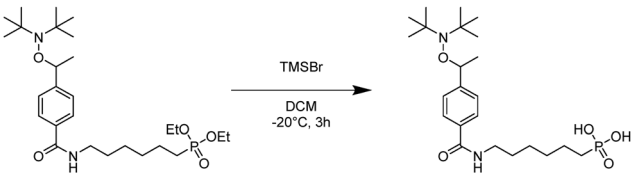

Synthesis of iron oxide nanoparticles IONP@OA/OL. The IONP@OA/OL nanoparticles of *ca.* 25 nm stabilized by oleate (OA) and oleyl amine (OL) were prepared by adapting the previously published procedure involving flash decomposition of the FeO(OH) precursor in *n*-docosane.[75] First, a mixture of FeO(OH) (2.1 mmol, 0.186 g), oleic acid (10 mmol, 3.17 g) and *n*-docosane (5.02 g) was dried under vacuum for 30 min at room temperature. The mixture was heated to 350 °C under argon flow with a heating rate of 10 °C min^{-1} and the temperature was maintained for a further 90 min under stirring. Then the temperature was cooled down to 200 °C, the system was open to air and the temperature was maintained at

180 °C for a further 90 min to realize the oxidation of FeO nanoparticles to Fe_3O_4. The temperature was decreased to 50 °C and cyclohexane (15 mL) was added to precipitate the nanoparticles. The obtained solid was washed two times by dispersing in diethyl ether, followed by precipitation with ethanol (1 : 1 v/v), and then recovered using centrifugation (20 000 rpm, 10 min). Oleylamine (200 μL) was added to the collected material as an additional stabilizer. The resultant oleate/oleylamine-capped IONP/OA/OL nanoparticles were finally dispersed in THF (15 mL) for storage.[48]

Synthesis of IONP@alkoxyamine. The grafting of the alkoxyamine derivative (6-(4-(1-((di-*tert*-butylamino)oxy)ethyl)benzamido)hexyl) phosphonic acid on the surface of IONP/OA/OL was performed by a ligand exchange method thanks to the pendant phosphonate groups of alkoxyamine.[48] For this, 200 mg of (6-(4-(1-((di-*tert*-butylamino)oxy)ethyl)benzamido)hexyl) phosphonic acid was dissolved in 20 mL of THF/MeOH (95/5 (vol%)), and mixed with a suspension of 1 mg mL^{-1} of IONP/OA/OL in 20 mL THF. The mixture was then sonicated for 10 min and rotary stirred at 300 rpm at room temperature for 48 hours. The as-obtained IONP@alkoxyamine nanoparticles were then collected by magnetic separation and washed three times with MeOH. The nanoparticles were then stored in MeOH or dried for further characterization.

Characterization

Transmission electronic microscopy (TEM) measurements were performed by using a LaB6 JEOL 1400 Flash electronic microscope at 100 kV. Dynamic light scattering (DLS) measurements were performed on a Zetasizer Nano-series Malvern instrument (ZEN3600) in order to determine the hydrodynamic diameter of the nanoparticles. Powder X-ray diffraction (PXRD) was performed using a PANalytical X'Pert powder analytical diffractometer mounted in a Debye–Scherrer configuration and equipped with a Cu radiation source (λ = 1.5418 Å). Infrared spectra using attenuated total reflectance (ATR-IR) were recorded using a PerkinElmer spectrum two FT-IR Spectrometer. Quantifications of P and Fe elements were performed using a scanning electron microscope equipped with an energy dispersive X-ray analyser (SEM-EDX) on a FEI quanta FEG 200 instrument. The powders were deposited on an adhesive carbon film and analysed under vacuum. ^{1}H nuclear magnetic resonance (NMR) spectra were recorded using an internal deuterium lock at ambient temperatures on the following instrument: Bruker AC400 (400 MHz). Data were presented as follows: chemical shift (in ppm), integration, multiplicity (s = singlet, d = doublet, t = triplet, m = multiplet, br means the signal is broad, and dd = doublet of doublets), coupling constant (J in Hz) and integration. ^{13}C nuclear magnetic resonance (NMR) spectra were recorded using an internal deuterium lock at ambient temperatures on the following instrument: Bruker AC400 (101 MHz). ^{31}P nuclear magnetic resonance (NMR) spectra were recorded on a Bruker AC400 (162 MHz) spectrometer with complete proton decoupling. High-resolution mass spectra (HRMS) were performed on a SYNAPT G2 HDMS (Waters) spectrometer equipped with an atmospheric pressure ionization source (API) pneumatically assisted. Samples were ionized by positive electrospray mode as follows: electrospray tension (ISV): 2800 V; opening tension (OR): 20 V; and nebulization gas pressure (nitrogen): 800 L h^{-1}. Low resolution mass spectra were recorded on an ion trap AB SCIEX 3200 QTRAP equipped with an electrospray source. The parent ion (M^+, $[M + H]^+$, $[M + Na]^+$ or $[M + NH_4]^+$) is quoted.

Magnetothermia measurements

Magnetothermia measurements were carried out using an ac magnetic field generator (UltraFlex) at 340 kHz. The generated magnetic field is around 20 mT (16 kA m^{-1}). The samples were measured in the liquid state. A thermal camera OPTRIS PI 450i and/or an optic fibre was used to record the temperature elevation. They provide very similar results.

Photothermal measurements

The photothermal efficiency was measured by placing 300 μL of a colloidal solution in a quartz tube placed in a quartz cuvette. The cuvette was then placed in line with the laser, which irradiated at 808 nm with a power of 2.6 W cm^{-2}. An optic fibre enabling the temperature reading each 30 seconds was placed in the solution. The ΔT values were extracted after 10 minutes of exposure to the external stimuli (magnetic field or laser irradiation).

EPR investigations of the radical formation

EPR was performed using the Elexsys E500 CW spectrometer from Bruker, in the X band (around 9.8 GHz), equipped with a resonant cavity ER4122SHQ. Samples were analysed using 50 μL capillary tubes (from Hirschmann), sealed with silicon paste. Samples were carefully placed at the same positions. Analyses were made at room temperature, with a window of 10 mT (100 G) centred around g = 2, an amplitude of 1 G, a frequency of 100 kHz, and a microwave power of 10 db.

Radical release simulations

The radical release simulations were conducted by employing the solution of eqn (5) and (6), in conjunction with eqn (7) and (8). A custom-built Python routine was created to solve these equations numerically, utilising the "*solve_ivp*" function from the "*scipy.integrate*" package. The optimisation of the fit parameters was achieved through the use of the "*curve_fit*" function from the "*scipy.optimize*" library.

Photothermal modelling

The photothermal modelling was conducted using the COMSOL software,[76] which was employed for the purpose of solving the heat equation. The COMSOL software facilitated the incorporation of shape and volume aspects pertaining to the experimental sample. The sample was not regarded as isolated, and the thermal flux was optimized at its surfaces to facilitate the modelling of the temperature plateau. The light-to-heat conversion coefficient was employed as a fitting parameter within the power source term of the heat equation. Furthermore, the

light absorption at 808 nm of the sample was also optimised in order to enhance the precision of the fit result. Three experimental curves were optimized simultaneously in order to obtain an accurate value for the light-to-heat conversion parameter.

Conclusions

In summary, this article reports on a novel nano-system capable of providing localized radical release, remotely triggered by two external stimuli, AMF and laser irradiation, through a cascade of actions. The system consists of iron oxide nanoparticles covalently grafted with a thermosensitive alkoxyamine derivative, specifically (6-(4-(1-((di-*tert*-butylamino)oxy)ethyl) benzamido)hexyl)phosphonic acid. The originality of our approach lies in the unique advantages of alkoxyamines, which offer the ability to generate radicals upon local heating, with tunable activation energy. Additionally, they exhibit significant stability in the absence of external stimuli and can be chemically modified, enabling their grafting onto IONP surfaces. Upon exposure of IONP@alkoxyamine nanoparticles to 340 kHz AMF or 808 nm light irradiation, significant heating occurs on the nanoparticle surface, leading to the homolysis of the thermosensitive C–ON bond in the alkoxyamine and subsequent radical formation in an oxygen-independent manner.

The macroscopic magnetothermal heating of colloidal nanoparticle solutions was investigated, with a view to determining the impact of variables such as nanoparticle concentrations, AMF strength and solvent properties on heat transfer. In particular, our findings show that besides well investigated dependence on the concentration of nanoparticles and AMF parameters, the boiling point, viscosity, and specific heat of the solvent significantly influence the heating behaviour during magnetothermal experiments. In addition to magnetothermal activation, we investigated photothermal triggering under 808 nm light irradiation, demonstrating a substantial temperature increase that is dependent on the nanoparticle concentration.

The formation of radicals under both external stimuli was confirmed using EPR spectroscopy. The kinetics of radical release revealed for the first time that light irradiation at 808 nm (2.6 W cm^{-2}) allowed efficient radical release from grafted nanoparticles at 44 °C ($t_{1/2}$ = 24 min), whereas 20 h is needed for free alkoxyamine to show the same release at this temperature underscoring the potential for controlled radical release at relatively low temperatures. Moreover, AMF exposure accelerates the homolysis of IONP@alkoxyamine (16 kA m^{-1}, 2.9 mg mL^{-1}) twofold compared to the free alkoxyamine at 77 °C ($t_{1/2}$ = 9 min *vs.* 18 min).

Importantly, this study demonstrated that the homolysis rate on the surface of the nanoparticles under external stimuli is significantly higher than expected based on bulk heating alone. This pronounced difference underscores the importance of nanoscale effects, which could arise from either very localized heating in the corona of the nanoparticle surface or catalytic processes triggered by alternating magnetic field (AMF) or light irradiation. Notably, homolysis of the alkoxyamine did not occur in the absence of nanoparticles when free alkoxyamines were subjected to external stimuli. The efficient radical generation observed during both AMF and laser irradiation indicates that these nanoscale interactions play a critical role in enhancing the reaction rates of the thermosensitive alkoxyamines, with this effect being much more pronounced under light irradiation.

The results suggest that the IONP@alkoxyamine system not only provides a platform for controlled radical release but also highlights the potential for leveraging nanoscale phenomena to optimize radical generation in various applications. By harnessing the unique thermal and catalytic properties of this system, we can achieve efficient radical release under mild conditions, making it particularly promising for diverse applications. Future investigations should aim to further elucidate the mechanisms driving these nanoscale effects, ultimately enhancing the capabilities of this innovative nanomaterial system. Moreover, exploring water-soluble alkoxyamine decorated IONPs would be highly relevant for biomedical magneto-photothermia applications.

Author contributions

Conceptualization, G. A., S. M., J. L. and Y. G.; methodology, G. A., S. M., J. L. and G. F.; software, G. F.; validation, S. S., F. A. S., B. B., P. J. and E. A.; investigation, F. A. S., S. S., B. B. and J. H. resources, G. A., S. M., J. L., and Y. G.; data curation, F. A. S., B. B. and E. A., J.-P. J., and E. O.; writing – original draft preparation, J. L., G. F., F. and A. S.; writing – review and editing, A. G., S. M., J. L., F. A. S., G. F. and Y. G.; visualization, S. S., G. F., B. B. and J. H.; supervision, S. S., G. F., A. G., S. M., J.-P. J., J. L. and Y. G.; project administration, A. G., S. M., J. L. and Y. G.; and funding acquisition, A. G., S. M., J. L. and Y. G.

Data availability

All data generated or analyzed during this study are included in the main article or in the supplementary information files accompanying this article. Additional details and data that support the findings of this study are available from the corresponding author upon reasonable request. For further information, please contact Pr. Joulia Larionova at joulia.larionova@umontpellier.fr and/or Pr. Sylvain Marque at sylvain.marque@univ-amu.fr.

Conflicts of interest

There are no conflicts to declare.

Acknowledgements

The authors thank the University of Montpellier, the University of Aix Marseille and CNRS for financial support. This work was developed within the scope of the ANR projects Killer (ANR-22-CE09-0026), and the authors are grateful for funding. The authors are grateful to Platform of Analysis and Characterization

(UAR2041) for magnetic, EPR, elemental analysis, TEM, EDS, SEM, and X-ray diffraction measurements.

Notes and references

1 M. Moros, J. Idiago-López, L. Asín, E. Moreno-Antolín, L. Beola, V. Grazú, R. M. Fratila, L. Gutiérrez and J. M. de la Fuente, Triggering antitumoural drug release and gene expression by magnetic hyperthermia, *Adv. Drug Delivery Rev.*, 2019, **138**, 326–343.

2 J. F. Liu, B. Jang, D. Issadore and A. Tsourkas, Use of magnetic fields and nanoparticles to trigger drug release and improve tumor targeting, *Wiley Interdiscip. Rev.: Nanomed. Nanobiotechnol.*, 2019, **11**, e1571.

3 J. Chen, Y. Zhu, C. Wu and J. Shi, Nanoplatform-based cascade engineering for cancer therapy, *Chem. Soc. Rev.*, 2020, **49**, 9057–9094.

4 S. Mura, J. Nicolas and P. Couvreur, Stimuli-responsive nanocarriers for drug delivery, *Nat. Mater*, 2013, **12**, 991–1003.

5 S. Su and P. M. Kang, Recent Advances in Nanocarrier-Assisted Therapeutics Delivery Systems, *Pharmaceutics*, 2020, **12**, 837.

6 Y. Zhang, Y. Wang, Q. Zhou, X. Chen, W. Jiao, G. Li, M. Peng, X. Liu, Y. He and H. Fan, Precise Regulation of Enzyme–Nanozyme Cascade Reaction Kinetics by Magnetic Actuation toward Efficient Tumor Therapy, *ACS Appl. Mater. Interfaces*, 2021, **13**, 52395–52405.

7 R. Jauregui, S. Srinivasan, L. N. Vojtech, H. S. Gammill, D. T. Chiu, F. Hladik, P. S. Stayton and J. J. Lai, Temperature-Responsive Magnetic Nanoparticles for Enabling Affinity Separation of Extracellular Vesicles, *ACS Appl. Mater. Interfaces*, 2018, **10**, 33847–33856.

8 Q. M. Kainz and O. Reiser, Polymer- and Dendrimer-Coated Magnetic Nanoparticles as Versatile Supports for Catalysts, Scavengers, and Reagents, *Acc. Chem. Res.*, 2014, **47**, 667–677.

9 Y. Lim, S. Noh, T.-H. Shin, J. Lee, D. Lungerich, J.-H. Lee and J. Cheon, Magnetothermally Activated Nanometer-level Modular Functional Group Grafting of Nanoparticles, *Nano Lett.*, 2021, **21**, 3649–3656.

10 J. G. Ovejero, I. Armenia, D. Serantes, S. Veintemillas-Verdaguer, N. Zeballos, F. López-Gallego, C. Grüttner, J. M. de la Fuente, M. del Puerto Morales and V. Grazu, Selective Magnetic Nanoheating: Combining Iron Oxide Nanoparticles for Multi-Hot-Spot Induction and Sequential Regulation, *Nano Lett.*, 2021, **21**, 7213–7220.

11 H. Gavilán, S. K. Avugadda, T. Fernández-Cabada, N. Soni, M. Cassani, B. T. Mai, R. Chantrell and T. Pellegrino, Magnetic nanoparticles and clusters for magnetic hyperthermia: optimizing their heat performance and developing combinatorial therapies to tackle cancer, *Chem. Soc. Rev.*, 2021, **50**, 11614–11667.

12 P. Guardia, A. Riedinger, S. Nitti, G. Pugliese, S. Marras, A. Genovese, M. E. Materia, C. Lefevre, L. Manna and T. Pellegrino, One pot synthesis of monodisperse water soluble iron oxide nanocrystals with high values of the specific absorption rate, *J. Mater. Chem. B*, 2014, **2**, 4426–4434.

13 G. Salas, J. Camarero, D. Cabrera, H. Takacs, M. Varela, R. Ludwig, H. Dähring, I. Hilger, R. Miranda, M. del, P. Morales and F. J. Teran, Modulation of Magnetic Heating via Dipolar Magnetic Interactions in Monodisperse and Crystalline Iron Oxide Nanoparticles, *J. Phys. Chem. C*, 2014, **118**, 19985–19994.

14 J.-P. Fortin, C. Wilhelm, J. Servais, C. Ménager, J.-C. Bacri and F. Gazeau, Size-Sorted Anionic Iron Oxide Nanomagnets as Colloidal Mediators for Magnetic Hyperthermia, *J. Am. Chem. Soc.*, 2007, **129**, 2628–2635.

15 L. Storozhuk, M. O. Besenhard, S. Mourdikoudis, A. P. LaGrow, M. R. Lees, L. D. Tung, A. Gavriilidis and N. T. K. Thanh, Stable Iron Oxide Nanoflowers with Exceptional Magnetic Heating Efficiency: Simple and Fast Polyol Synthesis, *ACS Appl. Mater. Interfaces*, 2021, **13**, 45870–45880.

16 E. R. Aluri, S. D. Shingte, E. P. McKiernan, S. Ferguson and D. F. Brougham, Modulation of hyperthermic and relaxometric responses of magnetic iron oxide nanoparticles through ligand exchange provides design criteria for dual-functionality, *J. Mater. Chem. C*, 2023, **11**, 6417–6428.

17 A. V. de Walle, A. Figuerola, A. Espinosa, A. Abou-Hassan, M. Estrader and C. Wilhelm, Emergence of magnetic nanoparticles in photothermal and ferroptotic therapies, *Mater. Horiz.*, 2023, **10**, 4757–4775.

18 A. G. Roca, J. F. Lopez-Barbera, A. Lafuente, F. Özel, E. Fantechi, J. Muro-Cruces, M. Hémadi, B. Sepulveda and J. Nogues, Iron oxide nanoparticles (Fe_3O_4, γ-Fe_2O_3 and FeO) as photothermal heat mediators in the first, second and third biological windows, *Phys. Rep.*, 2023, **1043**, 1–35.

19 A. Turki Jalil, M. A. Abdulhadi, L. R. Al-Ameer, O. F. Washeel, S. J. Abdulameer, M. S. Merza, M. Abosaooda and A. A. Mahdi, Free radical based nano cancer therapy, *J. Drug Delivery Sci. Technol.*, 2023, **87**, 104803.

20 J. Liu, B. Jia, Z. Li and W. Li, Reactive oxygen species-responsive polymer drug delivery systems, *Front. Bioeng. Biotechnol.*, 2023, **11**, 1115603.

21 R. S. Chasara, T. O. Ajayi, D. M. Leshilo, M. S. Poka and B. A. Witika, Exploring novel strategies to improve anti-tumour efficiency: the potential for targeting reactive oxygen species, *Heliyon*, 2023, **9**, e19896.

22 M. Overchuk, R. A. Weersink, B. C. Wilson and G. Zheng, Photodynamic and Photothermal Therapies: Synergy Opportunities for Nanomedicine, *ACS Nano*, 2023, **17**, 7979–8003.

23 S. Shi, L. Zhang, M. Zhu, G. Wan, C. Li, J. Zhang, Y. Wang and Y. Wang, Reactive Oxygen Species-Responsive Nanoparticles Based on PEGlated Prodrug for Targeted Treatment of Oral Tongue Squamous Cell Carcinoma by Combining Photodynamic Therapy and Chemotherapy, *ACS Appl. Mater. Interfaces*, 2018, **10**, 29260–29272.

24 O. Guselnikova, S. R. A. Marque, E. V. Tretyakov, D. Mares, V. Jerabek, G. Audran, J.-P. Joly, M. Trusova, V. Svorcik,

O. Lyutakov and P. Postnikov, Unprecedented plasmon-induced nitroxide-mediated polymerization (PI-NMP): a method for preparation of functional surfaces, *J. Mater. Chem. A*, 2019, **7**, 12414–12419.

25 X. Meng, L. Li, Y. Huang, X. Deng, X. Liu and Z. Li, Upconversion nanoparticle-assisted cationic and radical/cationic hybrid photopolymerization using sulfonium salts, *Polym. Chem.*, 2021, **12**, 7005–7009.

26 W. Zhou, M. Du, J. Wang, X. Zhang, T. Liang, C. Xie and Q. Fan, Organic nanomaterials for near-infrared light-triggered photothermal/thermodynamic combination therapy, *Dyes Pigm.*, 2022, **205**, 110499.

27 J. Xiao, H. Cong, S. Wang, B. Yu and Y. Shen, Recent research progress in the construction of active free radical nanoreactors and their applications in photodynamic therapy, *Biomater. Sci.*, 2021, **9**, 2384–2412.

28 G. Huang, Y. Qiu, F. Yang, J. Xie, X. Chen, L. Wang and H. Yang, Magnetothermally Triggered Free-Radical Generation for Deep-Seated Tumor Treatment, *Nano Lett.*, 2021, **21**, 2926–2931.

29 H. Hu, X. Deng, Q. Song, W. Yang, Y. Zhang, W. Liu, S. Wang, Z. Liang, X. Xing, J. Zhu, J. Zhang, Z. Shao, B. Wang and Y. Zhang, Mitochondria-targeted accumulation of oxygen-irrelevant free radicals for enhanced synergistic low-temperature photothermal and thermodynamic therapy, *J. Nanobiotechnology*, 2021, **19**, 390.

30 X. Li, Y. Liu, F. Fu, M. Cheng, Y. Liu, L. Yu, W. Wang, Y. Wan and Z. Yuan, Single NIR Laser-Activated Multifunctional Nanoparticles for Cascaded Photothermal and Oxygen-Independent Photodynamic Therapy, *Nano-Micro Lett.*, 2019, **11**, 68.

31 D. Ding, Z. Mei, H. Huang, W. Feng, L. Chen, Y. Chen and J. Zhou, Oxygen-Independent Sulfate Radical for Stimuli-Responsive Tumor Nanotherapy, *Adv. Sci.*, 2022, **9**, 2200974.

32 J. Yang, R. Xie, L. Feng, B. Liu, R. Lv, C. Li, S. Gai, F. He, P. Yang and J. Lin, Hyperthermia and Controllable Free Radical Coenhanced Synergistic Therapy in Hypoxia Enabled by Near-Infrared-II Light Irradiation, *ACS Nano*, 2019, **13**, 13144–13160.

33 S. Ning, Z. Liu, M. Chen, D. Zhu and Q. Huang, Nanozyme hydrogel for enhanced alkyl radical generation and potent antitumor therapy, *Nanoscale Adv.*, 2022, **4**, 3950–3956.

34 E. Ximendes, R. Marin, Y. Shen, D. Ruiz, D. Gómez-Cerezo, P. Rodríguez-Sevilla, J. Lifante, P. X. Viveros-Méndez, F. Gámez, D. García-Soriano, G. Salas, C. Zalbidea, A. Espinosa, A. Benayas, N. García-Carrillo, L. Cussó, M. Desco, F. J. Teran, B. H. Juárez and D. Jaque, Infrared-Emitting Multimodal Nanostructures for Controlled In Vivo Magnetic Hyperthermia, *Adv. Mater.*, 2021, **33**, 2100077.

35 K. El-Boubbou, E. Ximendes, F. J. Teran, R. Marin, Á. Artiga, D. H. Ortgies and D. Jaque, PEGylated Opto-Magnetic Gold and Silver Sulfide Iron Oxide Nanoprobes for Synergistic Photothermal Therapy, *ACS Appl. Nano Mater.*, 2024, **7**, 13959–13972.

36 L. Feng, S. Gai, Y. Dai, F. He, C. Sun, P. Yang, R. Lv, N. Niu, G. An and J. Lin, Controllable Generation of Free Radicals from Multifunctional Heat-Responsive Nanoplatform for Targeted Cancer Therapy, *Chem. Mater.*, 2018, **30**, 526–539.

37 H. Xiang, H. Lin, L. Yu and Y. Chen, Hypoxia-Irrelevant Photonic Thermodynamic Cancer Nanomedicine, *ACS Nano*, 2019, **13**, 2223–2235.

38 X.-Q. Wang, F. Gao and X.-Z. Zhang, Initiator-Loaded Gold Nanocages as a Light-Induced Free-Radical Generator for Cancer Therapy, *Angew. Chem., Int. Ed.*, 2017, **56**, 9029–9033.

39 F. Wang, Z. Sun, Z. Wang, J. Zhou and L. Sun, PdAu-based nanotheranostic agent for photothermally initiated and oxygen-independent free radical generation, *CrystEngComm*, 2022, **24**, 5090–5096.

40 D. Cao, H. He, W. Li, J. Yan, J. Wu, M. Yin, Y. Zhou, Z. Zhou and L. Yin, A near-infrared light-controlled, oxygen-independent radical generating nano-system toward cancer therapy, *Biomater. Sci.*, 2021, **9**, 4054–4065.

41 S. Li, M. Qi, Q. Yang, F. Shi, C. Liu, J. Du, Y. Sun, C. Li and B. Dong, State-of-the-Art on the Sulfate Radical-Advanced Oxidation Coupled with Nanomaterials: Biological and Environmental Applications, *J. Funct. Biomater.*, 2022, **13**, 227.

42 W. Li, B. Li, B. Wu, B. Tian, X. Chen, C. Wang, W. Hong and J. Peng, Free-Radical Cascade Generated by AIPH/Fe_3O_4-Coloaded Nanoparticles Enhances MRI-Guided Chemo/Thermodynamic Hypoxic Tumor Therapy, *ACS Appl. Mater. Interfaces*, 2022, **14**, 29563–29576.

43 G. Audran, S. R. A. Marque and P. Mellet, Smart Alkoxyamines: A New Tool for Smart Applications, *Acc. Chem. Res.*, 2020, **53**, 2828–2840.

44 P. Brémond, A. Koïta, S. R. A. Marque, V. Pesce, V. Roubaud and D. Siri, Chemically Triggered C–ON Bond Homolysis of Alkoxyamines. Quaternization of the Alkyl Fragment, *Org. Lett.*, 2012, **14**, 358–361.

45 G. Audran, E. G. Bagryanskaya, S. R. A. Marque and P. Postnikov, New Variants of Nitroxide Mediated Polymerization, *Polymers*, 2020, **12**, 1481.

46 M. Edeleva, G. Audran, S. Marque and E. Bagryanskaya, Smart Control of Nitroxide-Mediated Polymerization Initiators' Reactivity by pH, Complexation with Metals, and Chemical Transformations, *Materials*, 2019, **12**, 688.

47 D. Bertin, D. Gigmes, S. R. A. Marque and P. Tordo, Kinetic subtleties of nitroxide mediated polymerization, *Chem. Soc. Rev.*, 2011, **40**, 2189–2198.

48 B. Bouvet, S. Sene, G. Félix, J. Havot, G. Audran, S. R. A. Marque, J. Larionova and Y. Guari, Cascade strategy for triggered radical release by magnetic nanoparticles grafted with thermosensitive alkoxyamine, *Nanoscale*, 2022, **15**, 144–153.

49 A. Lak, D. Niculaes, G. C. Anyfantis, G. Bertoni, M. J. Barthel, S. Marras, M. Cassani, S. Nitti, A. Athanassiou, C. Giannini and T. Pellegrino, Facile transformation of FeO/Fe_3O_4 core-shell nanocubes to Fe_3O_4 via magnetic stimulation, *Sci. Rep.*, 2016, **6**, 33295.

50 B. Leszczyński, G. C. Hadjipanayis, A. A. El-Gendy, K. Załęski, Z. Śniadecki, A. Musiał, M. Jarek, S. Jurga and A. Skumiel, The influence of oxidation process on exchange

bias in egg-shaped FeO/Fe_3O_4 core/shell nanoparticles, *J. Magn. Magn. Mater.*, 2016, **416**, 269–274.
51 X. Sun, N. Frey Huls, A. Sigdel and S. Sun, Tuning Exchange Bias in Core/Shell FeO/Fe_3O_4 Nanoparticles, *Nano Lett.*, 2012, **12**, 246–251.
52 X. Batlle, N. Pérez, P. Guardia, O. Iglesias, A. Labarta, F. Bartolomé, L. M. García, J. Bartolomé, A. G. Roca, M. P. Morales and C. J. Serna, Magnetic nanoparticles with bulklike properties (invited), *J. Appl. Phys.*, 2011, **109**, 07B524.
53 K. Jiang, Q. Zhang, D. T. Hinojosa, L. Zhang, Z. Xiao, Y. Yin, S. Tong, V. L. Colvin and G. Bao, Controlled oxidation and surface modification increase heating capacity of magnetic iron oxide nanoparticles, *Appl. Phys. Rev.*, 2021, **8**, 031407.
54 A. Espinosa, R. Di Corato, J. Kolosnjaj-Tabi, P. Flaud, T. Pellegrino and C. Wilhelm, Duality of Iron Oxide Nanoparticles in Cancer Therapy: Amplification of Heating Efficiency by Magnetic Hyperthermia and Photothermal Bimodal Treatment, *ACS Nano*, 2016, **10**, 2436–2446.
55 R. R. Wildeboer, P. Southern and Q. A. Pankhurst, On the reliable measurement of specific absorption rates and intrinsic loss parameters in magnetic hyperthermia materials, *J. Phys. D: Appl. Phys.*, 2014, **47**, 495003.
56 O. L. Lanier, O. I. Korotych, A. G. Monsalve, D. Wable, S. Savliwala, N. W. F. Grooms, C. Nacea, O. R. Tuitt and J. Dobson, Evaluation of magnetic nanoparticles for magnetic fluid hyperthermia, *Int. J. Hyperthermia*, 2019, **36**, 687–701.
57 Z. J. Díaz-Puerto, Á. Raya-Barón, P. W. N. M. van Leeuwen, J. M. Asensio and B. Chaudret, Determination of the surface temperature of magnetically heated nanoparticles using a catalytic approach, *Nanoscale*, 2021, **13**, 12438–12442.
58 M. Vassallo, D. Martella, G. Barrera, F. Celegato, M. Coïsson, R. Ferrero, E. S. Olivetti, A. Troia, H. Sözeri, C. Parmeggiani, D. S. Wiersma, P. Tiberto and A. Manzin, Improvement of Hyperthermia Properties of Iron Oxide Nanoparticles by Surface Coating, *ACS Omega*, 2023, **8**, 2143–2154.
59 O. M. Lemine, N. Madkhali, M. Alshammari, S. Algessair, A. Gismelseed, L. El Mir, M. Hjiri, A. A. Yousif and K. El-Boubbou, Maghemite (γ-Fe_2O_3) and γ-Fe_2O_3–TiO_2 Nanoparticles for Magnetic Hyperthermia Applications: Synthesis, Characterization and Heating Efficiency, *Materials*, 2021, **14**, 5691.
60 D. Serantes, K. Simeonidis, M. Angelakeris, O. Chubykalo-Fesenko, M. Marciello, M. del, P. Morales, D. Baldomir and C. Martinez-Boubeta, Multiplying Magnetic Hyperthermia Response by Nanoparticle Assembling, *J. Phys. Chem. C*, 2014, **118**, 5927–5934.
61 D. Cabrera, J. Camarero, D. Ortega and F. J. Teran, Influence of the aggregation, concentration, and viscosity on the nanomagnetism of iron oxide nanoparticle colloids for magnetic hyperthermia, *J. Nanopart. Res.*, 2015, **17**, 121.
62 A. Rousseau, M. Tellier, L. Marin, M. Garrow, C. Madelaine, N. Hallali and J. Carrey, Influence of medium viscosity on the heating power and the high-frequency magnetic properties of nanobeads containing magnetic nanoparticles, *J. Magn. Magn. Mater.*, 2021, **518**, 167403.
63 M. E. Sadat, M. Kaveh Baghbador, A. W. Dunn, H. P. Wagner, R. C. Ewing, J. Zhang, H. Xu, G. M. Pauletti, D. B. Mast and D. Shi, Photoluminescence and photothermal effect of Fe_3O_4 nanoparticles for medical imaging and therapy, *Appl. Phys. Lett.*, 2014, **105**, 091903.
64 A. Espinosa, J. Kolosnjaj-Tabi, A. Abou-Hassan, A. Plan Sangnier, A. Curcio, A. K. A. Silva, R. Di Corato, S. Neveu, T. Pellegrino, L. M. Liz-Marzán and C. Wilhelm, Magnetic (Hyper)Thermia or Photothermia? Progressive Comparison of Iron Oxide and Gold Nanoparticles Heating in Water, in Cells, and In Vivo, *Adv. Funct. Mater.*, 2018, **28**, 1803660.
65 S. Cabana, A. Curcio, A. Michel, C. Wilhelm and A. Abou-Hassan, Iron Oxide Mediated Photothermal Therapy in the Second Biological Window: A Comparative Study between Magnetite/Maghemite Nanospheres and Nanoflowers, *Nanomaterials*, 2020, **10**, 1548.
66 C. Lozano-Pedraza, E. Plaza-Mayoral, A. Espinosa, B. Sot, A. Serrano, G. Salas, C. Blanco-Andujar, G. Cotin, D. Felder-Flesch, S. Begin-Colin and F. J. Teran, Assessing the parameters modulating optical losses of iron oxide nanoparticles under near infrared irradiation, *Nanoscale Adv.*, 2021, **3**, 6490–6502.
67 S. Marque, Influence of the Nitroxide Structure on the Homolysis Rate Constant of Alkoxyamines: A Taft−Ingold Analysis, *J. Org. Chem.*, 2003, **68**, 7582–7590.
68 J. Marbaix, N. Mille, L.-M. Lacroix, J. M. Asensio, P.-F. Fazzini, K. Soulantica, J. Carrey and B. Chaudret, Tuning the Composition of FeCo Nanoparticle Heating Agents for Magnetically Induced Catalysis, *ACS Appl. Nano Mater.*, 2020, **3**, 3767–3778.
69 E. Cazares-Cortes, S. Cabana, C. Boitard, E. Nehlig, N. Griffete, J. Fresnais, C. Wilhelm, A. Abou-Hassan and C. Ménager, Recent insights in magnetic hyperthermia: from the 'hot-spot' effect for local delivery to combined magneto-photo-thermia using magneto-plasmonic hybrids, *Adv. Drug Delivery Rev.*, 2019, **138**, 233–246.
70 J. Dong and J. I. Zink, Taking the Temperature of the Interiors of Magnetically Heated Nanoparticles, *ACS Nano*, 2014, **8**, 5199–5207.
71 H. Huang, S. Delikanli, H. Zeng, D. M. Ferkey and A. Pralle, Remote control of ion channels and neurons through magnetic-field heating of nanoparticles, *Nat. Nanotechnol.*, 2010, **5**, 602–606.
72 A. Riedinger, P. Guardia, A. Curcio, M. A. Garcia, R. Cingolani, L. Manna and T. Pellegrino, Subnanometer Local Temperature Probing and Remotely Controlled Drug Release Based on Azo-Functionalized Iron Oxide Nanoparticles, *Nano Lett.*, 2013, **13**, 2399–2406.
73 D. Liu, Y. Huang, J. Hu, B. Wang and Y. Lu, Multiscale Catalysis Under Magnetic Fields: Methodologies, Advances, and Trends, *ChemCatChem*, 2022, **14**, e202200889.
74 O. Guselnikova, G. Audran, J.-P. Joly, A. Trelin, E. V. Tretyakov, V. Svorcik, O. Lyutakov, S. R. A. Marque and P. Postnikov, Establishing plasmon contribution to

chemical reactions: alkoxyamines as a thermal probe, *Chem. Sci.*, 2021, **12**, 4154–4161.

75 W. W. Yu, J. C. Falkner, C. T. Yavuz and V. L. Colvin, Synthesis of monodisperse iron oxide nanocrystals by thermal decomposition of iron carboxylate salts, *Chem. Commun.*, 2004, 2306–2307.

76 COMSOL Multiphysics® v. 6.0, **https://www.comsol.com**. COMSOL AB, Stockholm, Sweden.